

A Spectroscopic and *ab initio* Study of the Hydrogen Peroxide–Formic Acid Complex

by

Leo Yuxiu Li

A thesis submitted in partial fulfillment of the requirements for the degree of

Master of Science

Department of Chemistry
University of Alberta

© Leo Yuxiu Li, 2018

ABSTRACT

The hydrogen-bonded complex between hydrogen peroxide and formic acid was studied by rotational spectroscopy and *ab initio* calculations. Because of the simplicity, chemical activity, and importance of hydrogen peroxide, it is a prototypical molecule to study intermolecular interactions, in particular hydrogen bonding. This work provides microscopic descriptions of the hydrogen peroxide–formic acid binary complex, which potentially could benefit much future work. Details of theories and experimental principles, including the setup of the cavity-based and chirped-pulse Fourier-transform spectrometers, are described. Also, a background of hydrogen peroxide and the reasons for studying its complex with formic acid are discussed. The results indicate that the most stable geometry of the hydrogen peroxide – formic acid binary complex includes a 7-membered ring-like hydrogen bonded structure, which is the only conformer found in the experimental work. In the spectrum of the complex a splitting of rotational transitions is observed, which is attributed to a tunneling motion of the non-hydrogen bonded hydrogen atom of hydrogen peroxide. Analyses of the electron density topology show that the complex is held together by two strong hydrogen bonds, where hydrogen peroxide slightly favors being a proton acceptor than a donor.

PREFACE

This thesis is based on the work I have done at the University of Alberta between January 2016 and March 2018. In this work, Professors W. Jäger and Y. Xu provided experimental guidance and helped to shape the concept. Dr. Nathan A. Seifert helped with the fitting of spectroscopic constants of the studied complex. Fan Xie helped with the *ab initio* search for the transition state and the intrinsic reaction coordinate calculations that are associated with the observed tunneling motion. The remaining parts, including the *ab initio* geometry searches and optimizations, recording of the spectra, sample preparations, data analyses, and writing of the thesis, were done by myself. The final manuscript to be submitted for publication is being polished with the help from Dr. Nathan A. Seifert and Professor W. Jäger.

ACKNOWLEDGEMENTS

I would like to express my sincerest gratitude towards my supervisor, Professor Wolfgang Jäger. Wolfgang is a very creative scientist with endless passion and energy. His critical thinking and detail-oriented manner are two most important characteristics that I have been inspired by. He is also an easy-going and open-minded person, who always puts his students first no matter how busy he is. Anyone who has had the privilege of working with Wolfgang would agree that he is a smart, excellent, and humorous role model.

I would like to acknowledge Professor Yunjie Xu for her supportive and valuable advice on the interpretation of experimental data. She is very knowledgeable and enthusiastic about science, especially in the area of rotational spectroscopy. Without her suggestions, many insights could not have been found proficiently. I am thankful to my committee members, Professor James Harynuk, Professor Gabriel Hanna, and Professor Alexander Brown, for their helpful suggestions. A big thank you to my teaching assistant coordinator, Dr. Anna D. Jordan, for the writing guidance and our friendship.

I also want to show my appreciations to my group members. Especially, I am grateful having had the chance to do my first measurements with Dr. Elijah G. Schnitzler. A ‘thank you’ to many other members, including Dr. Nathan A. Seifert, Dr. Matthias Heger, Dr. Prasanta Das, Dr. Javix Thomas, Chrissy Knapp, Joseph Cheramy, Angelo S. Perera, Amin Moazeni, Jiao Gao, Jason Huang, Fan Xie, Ningjie Sun, Boyang Zhao, Yanqing Yang, Bowei Wu, and Guojie Li, from whom I have learned a lot and shared discussions throughout my time in this group..

Finally, I am deeply indebted to the emotional support provided by my family and close friends. In particular, I am grateful to my loving parents and my sister. I would not have been able to finish this work without their infinite love and encouragement.

TABLE OF CONTENTS

CHAPTER 1 – Introduction	01
1.1 Motivation	02
1.2 Outline of Present Work	04
CHAPTER 2 – Details of the Theories and Experimental Principles	05
2.1 Rotational Spectroscopy	06
2.1.1 Semi-rigid Rotor Model	06
2.1.2 Non-linear Rotors	08
2.1.3 Rotational Transitions	10
2.1.4 Superposition States	11
2.1.5 Density Matrix Formalism	13
2.1.6 The Optical Bloch Equations	15
2.1.7 Solution of The Bloch Equations	17
2.2 Supersonic Jet Expansion	20
2.3 Microwave Spectrometers	22
2.3.1 The Cavity-based FTMW Spectrometer	23
2.3.2 The Chirped-pulse FTMW Spectrometer	28
2.4 Theoretical Calculations	32
2.4.1 <i>Ab initio</i> Wavefunction Calculations	32
2.4.2 <i>Ab initio</i> Density Functional Theory	33
2.5 Scientific Software	34

CHAPTER 3 – A Study of the Hydrogen Peroxide – Formic Acid Complex	35
3.1 Introduction	36
3.1.1 Hydrogen Peroxide and its Significance	36
3.1.2 An Appropriate Choice for the Study	38
3.2 Conformational Searches	39
3.3 Sample Preparation	42
3.4 Transition Assignments	44
3.4.1 The Closed-frequency Loop Method	45
3.4.2 Intensity Analyses and The Tunneling Splitting	46
3.5 Intrinsic Reaction Coordinate Calculations	51
3.6 Fitting of The Spectroscopic Constants	53
3.7 Analyses of the Electron Density Topology	54
3.7.1 Visualization of Non-Covalent Interactions	57
3.7.2 Hydrogen Bonding Evaluations	58
3.8 Summary	59
CHAPTER 4 – Concluding Remarks	60
BIBLIOGRAPHY	62
APPENDICES	80

LIST OF TABLES

<i>Table 3.2.1</i> Calculated spectroscopic constants for the lowest two HP-FA conformers	41
<i>Table 3.4.1</i> Frequencies (in MHz) of the a-type and b-type transitions of HP-FA-I	46
<i>Table 3.4.2</i> Frequencies (in MHz) of the observed interstate c-type transitions of HP-FA-I	51
<i>Table 3.6.1</i> The fitted spectroscopic constants of HP-FA-I	54
<i>Table 3.7.1</i> BCP properties and energy evaluation for H-bonds in HP-FA-I and HP-FA-I*	58
<i>Appendix A</i> – The Cartesian coordinates of the optimized geometry for HP-FA-I and HP-FA-I* calculated at the MP2/6-311++g(2d,p) level of theory.	81

LIST OF FIGURES

<i>Figure 2.1.1</i> Time evolution of the system in the presence of an external electromagnetic field; (a) a resonant $\pi/2$ pulse, and (b) a resonant π pulse.	18
<i>Figure 2.1.2</i> The coherence of system is oscillating between u and v components at the off-resonance frequency $\Delta\omega$	19
<i>Figure 2.2.1</i> An illustration of a supersonic jet expansion.	21
<i>Figure 2.3.1</i> A schematic diagram of the revised Balle–Flygare type FTMW spectrometer.	23
<i>Figure 2.3.2</i> A typical pulse sequence programed in the cavity-based FTMW spectrometer.	27
<i>Figure 2.3.3</i> A schematic diagram of the chirped-pulse FTMW spectrometer.	28
<i>Figure 2.3.4</i> A typical time sequence to control the chirped-pulse FTMW spectrometer.	31
<i>Figure 3.2.1</i> Six optimized structures of the HP–FA complex and their relative energies.	40
<i>Figure 3.3.1</i> A photo of the cavity-based FTMW spectrometer.	42

<i>Figure 3.3.2</i> Cross-section of the stainless-steel nozzle cap.	
.....	43
<i>Figure 3.4.1</i> A closed-frequency loop (in red) in the rotational levels ($v = 0$) of HP-FA-I.	
.....	45
<i>Figure 3.4.3</i> The $2(0, 2) \leftarrow 1(0, 1)$ transitions of HP-FA-I (averaged over 500 cycles).	
.....	47
<i>Figure 3.4.4</i> The energy-level diagram with all measured transitions of HP-FA-I.	
.....	49
<i>Figure 3.4.5</i> A stick spectrum of all lines recorded between 12 and 15 GHz.	
.....	50
<i>Figure 3.5.1</i> Transition state found and used in verifying the proposed tunneling motion.	
.....	52
<i>Figure 3.5.2</i> The intrinsic reaction coordinate for the tunneling motion in HP-FA-I.	
.....	52
<i>Figure 3.7.1</i> The critical points and the bond paths of HP-FA-I found in the QTAIM analysis.	
.....	56
<i>Figure 3.7.2</i> The weak interactions in HP-FA-I unveiled by an NCI analysis.	
.....	57

LIST OF SYMBOLS

ψ	time-independent wavefunction	E	energy
Ψ	time-dependent wavefunction	E_{HB}	hydrogen bond energy
Ψ_s	superposition state wavefunction	E_J, E_{JK}	rotational level energies
$ \Psi ^2$	probability density	ΔE_{rot}	rotational transition energy
a_N, b_N, c_i	probability amplitude	ΔE_{01}	magnitude of tunneling splitting
$Y_J^M(\theta, \phi)$	spherical harmonic function	I_A, I_B, I_C	principal moment of inertia
$P_J^{ M }$	Legendre polynomials	F_a, F_b, F_c	Coriolis coupling parameters
\hat{H}	Hamiltonian	D, H, d_J	centrifugal distortion constants
H_0^R, H_1^R	rigid-body rotational Hamiltonians	A, B, C	rotational constants
H^{CD}	centrifugal distortion Hamiltonian	A, B	regression coefficients
H^{CC}	Coriolis coupling Hamiltonian	$\vec{\mu}$	electric dipole moment
P_g	symmetric angular momentum	$\vec{\mu}_{b \leftarrow a}$	transition probability
ν	vibrational quantum number	μ_a, μ_b, μ_c	dipole moment components
J	rotational quantum number	R	ideal gas constant
M	magnetic quantum number	T	absolute temperature
K, K_a, K_c	rotational angular momentum	T_1, T_2	relaxation terms
	quantum numbers	t	time
$\vec{\varepsilon}$	external electric field	r	radial distance
\vec{k}	wave-vector of an electric field	h, \hbar	Plank's constants
ε_0	strength of an electric field	Q	quality factor
ϕ	phase of an electric field	Q_e	intrinsic reaction coordinate

ν_0	incident microwave frequency	s, w, u, v	Bloch parameters
$\Delta\nu_{cp}$	chirped frequency range	w_{eq}, w_0	equilibrium population difference
$\Delta\nu_m$	frequency of molecular signal	s	reduced electron density gradient
ω	frequency of an electric field	λ_2	2 nd eigenvalue of a Hessian matrix
ω_{ab}, ω_{21}	resonant frequency of two states	ρ	electron density
$\Delta\omega$	detuning frequency	$\nabla^2\rho$	Laplacian of electron density
χ	generalized Rabi frequency	$V(r)$	potential energy
\hat{O}	arbitrary macroscopic observable	$r(\text{O}\cdots\text{H})$	hydrogen bond length
\bar{P}	macroscopic polarization	cm^{-1}	wavenumber
$\underline{\rho}$	density matrix	Hz	hertz
$\tilde{\underline{\rho}}$	density matrix in a rotating frame	D	Debye
σ	standard deviation	J	Joule

LIST OF ABBREVIATIONS

A/D	analog-to-digital converter
AWG	arbitrary wave generator
BCP	bond critical point
BSSE	basis set superposition error
DDG	digital delay generator
FTIR	Fourier-transform infrared
FTMW	Fourier-transform microwave
GUI	graphic user interface
HF	Hartree–Fock
HP–FA	hydrogen peroxide – formic acid binary complex
IRC	intrinsic reaction coordinate
MP n	n -th order Møller–Plesset perturbation theory
NCI	non-covalent interaction
NMR	nuclear magnetic resonance
RWA	rotating wave approximation
PDRO	phase-locked dielectric resonator oscillator
ppbv	parts per billion by volume
QTAIM / AIM	quantum theory of atoms in molecules
SOA	secondary organic aerosol
TTL	transistor-transistor logic
VMD	Visual Molecular Dynamics
ZPE	zero-point energy

CHAPTER 1

Introduction

1.1 Motivation

Many physical processes or properties, such as the condensation of gaseous molecules, the formation and aggregation of rain clouds [1], or the exceptionally high boiling point of water, can be explained if one knows how molecules or atoms attract one another, i.e. by knowing their intermolecular interactions. Intermolecular interactions play important roles in living systems. These interactions dictate, for example, the activities of enzymes or the structure of the DNA double helix. These examples indicate the importance of weak interactions present in the microscopic world.

An elegant way to learn about intermolecular interactions is through studies of van der Waals complexes [2]. A group of molecules or atoms that are weakly bound together by intermolecular interactions is called a van der Waals complex. Unlike traditional chemical bonds, where electrons are shared between atoms, these intermolecular interactions in a complex are established mainly through van der Waals forces [3], such as dispersion, induction, or permanent electric multipole–multipole interactions. Hydrogen bonding is a result mainly of dipole-dipole interactions, but other forces also play a role. Compared with the energy of a chemical bond, the binding energy of a van der Waals complex typically is at least a hundred times weaker; therefore, van der Waals complexes are unstable at room temperature. At low temperatures, van der Waals complexes can be formed in the gas phase by ternary collisions, where the third collision partner carries away the excess binding energy [2].

Hydrogen bonding is a relatively strong intermolecular interaction. Because of its importance in many fields of science, complexes held together by hydrogen bonding have been studied by various spectroscopic techniques, including Fourier-transform infrared (FTIR) spectroscopy [4-6], laser induced fluorescence spectroscopy [7-9], nuclear magnetic resonance (NMR) spectroscopy [10-12], etc. A particularly useful method to study hydrogen bonding is to probe rotational spectra

of van der Waals complexes that can be prepared in a pulsed molecular beam expansion. Fourier transform microwave spectrometers have very high-resolution capabilities so that fine- and hyperfine-structures of rotational transitions can be resolved. The resulting splitting contain copious information about molecular dynamics, e.g. tunnelling motions, and molecular structure.

Although van der Waals complexes have been studied by rotational spectroscopy for several decades, there remain still many unstudied systems. Hydrogen peroxide, an unstable but important small-sized molecule, is one such system whose complexes have not been studied in the gas phase. A main motivation for this study is to provide the first gas-phase high resolution rotational spectroscopic investigation of a complex that is based on a hydrogen peroxide subunit.

1.2 Outline of Present Work

The present work is divided into four chapters. In *Chapter 2*, details of the theories and experimental principles are reviewed. First, the theoretical framework of rotational spectroscopy and transition dynamics that will be used throughout the rest of document are given in *Section 2.1*, followed by the concept of the supersonic jet expansion in *Section 2.2*. The design details and operational principles of two types of instruments used in this study, including the cavity-based and chirped-pulse Fourier-transform microwave spectrometers, are presented in *Section 2.3*. In *Section 2.4*, the theoretical calculation methods used in this work are summarized. Several scientific software packages that were used for simulating or analyzing the experimental data are provided in the last part of this chapter, *Section 2.5*. The major focus of this work is concentrated in *Chapter 3*. An introduction to hydrogen peroxide and the reasons for studying it with formic acid as binding partner are discussed in *Section 3.1*. Preliminary studies in finding the optimized geometries of the complex and the sample preparation are covered in *Section 3.2* and *Section 3.3*, respectively. In *Section 3.4* to *Section 3.7*, spectroscopic assignments, data analyses, and interpretation of results are presented. A short summary of this project is given in *Section 3.8*. Finally, the concluding remarks of this work are stated in *Chapter 4*.

CHAPTER 2

Details of the Theories and Experimental Principles

2.1 Rotational Spectroscopy

Rotational spectroscopy is one of the high-resolution spectroscopic techniques where rotational transitions are targeted. A typical rotational transition is driven by microwave radiation, which is characterized by its wavelength from approximately 1 to 10^{-4} m (0.01 to 100 cm^{-1} ; 0.3 to 3000 GHz); therefore, rotational spectroscopy is also well-known as microwave spectroscopy. Much physical information of a molecule, such as its molecular structure and dynamics, can be obtained by measuring and analyzing its pure rotational spectrum [13]. The ‘pure’ rotational spectra are recorded by measuring only the transitions within the same vibrational and electronic state but between two different rotational states. In order to understand a specific application, as in the next chapter, some underlying principles of rotational spectroscopy are required. The following is merely a brief overview and by no means comprehensive. For significantly more detailed descriptions, the reader is encouraged to consult the references with that particular content.

2.1.1 Semi-rigid Rotor Model

In most cases, rotational spectra of molecules can be well-described by the semi-rigid rotor model [14], in which centrifugal distortions are considered on top of the rigid rotor model. The rigid rotor model of a diatomic molecule considers the end-over-end rotation of two-point masses, separated by a fixed distance, about their center of mass. Based on the postulates of quantum theory [15], rotational energy levels for a such system can be obtained by solving its time-independent Schrödinger equation:

$$\hat{H}\psi(q) = E\psi(q)$$

(Equation 2.1.1).

$\psi(q)$ in *Equation 2.1.1* is the spatial, time-independent wavefunction of the system. By choosing the rotational energy operator \hat{H} (Hamiltonian) in spherical coordinates, for its simplicity of representation, the form for a rigid rotor is:

$$\frac{\hbar}{2\hat{I}} \left[\frac{1}{\sin \theta} \frac{\partial}{\partial \theta} \left(\sin \theta \frac{\partial \psi(q)}{\partial \theta} \right) + \frac{1}{\sin^2 \theta} \frac{\partial^2 \psi(q)}{\partial \phi^2} \right] + E\psi(q) = 0$$

(*Equation 2.1.2*).

\hat{I} in *Equation 2.1.2* is the moment of inertia, a measurement of the resistance of a body to be rotated, whereas ψ stands for the rotational wavefunction and can be expressed as a function of two different angular coordinates, θ and ϕ ; so ψ can be rewritten as:

$$\psi = \Theta(\theta) \cdot \Phi(\phi)$$

(*Equation 2.1.3*).

By using the method of separation of variables, *Equation 2.1.2* can be solved to yield:

$$\psi = Y_J^M(\theta, \phi) = N_{Jm} \cdot P_J^{|M|} \cdot \cos \theta \cdot \exp[iM\phi], \text{ where}$$

$$J = 0, 1, 2, \dots; M = 0, \pm 1, \pm 2, \dots, \pm J$$

(*Equation 2.1.4*).

$Y_J^M(\theta, \phi)$ are known as spherical harmonics and are the set of rotational eigenfunctions with rotational quantum number J and magnetic quantum number M , in which N_{Jm} are normalization coefficients and $P_J^{|M|}$ are the associated Legendre polynomials [16]. The corresponding energies for a rigid rotor are given by:

$$E_J = \frac{\hbar}{2\hat{I}} J(J + 1) = BJ(J + 1)$$

(*Equation 2.1.5*).

In the above equation, B is the rotational constant, and E_J is the energy for the rotational level with rotational quantum number J . In other words, the energy for an arbitrary rotational level in the

rigid rotor model is independent of the magnetic quantum number M in the field-free case but only depends on the moment of inertia and the rotational quantum number J . Each rotational energy level, consequently, is $(2J + 1)$ -fold degenerate. The degeneracy can be removed by an external electric or magnetic field, i.e. by the Stark or Zeeman effect [17], respectively.

In almost all cases, the chemical bond, however, is not perfectly rigid so that a rotating molecule would experience centrifugal forces that pull the atoms apart, increasing the moment of inertia I , and decreasing the rotational constant B . To consider the effect of centrifugal distortions, correction terms can be added:

$$E_J = BJ(J + 1) - DJ^2(J + 1)^2 + HJ^3(J + 1)^3 + \dots$$

(Equation 2.1.6).

In Equation 2.1.6, D , H , or even higher order terms are centrifugal distortion constants. Notably, the inverse of D is proportional to the harmonic vibration frequency of the molecule.

2.1.2 Non-linear Rotors

In rotational spectroscopy, a set of principal axes (denoted by a , b , and c) of the moment of inertia tensor is conventionally chosen so that $I_A \leq I_B \leq I_C$ is satisfied. Based on their principal moments of inertia, molecules are categorized into five classes:

- linear tops ($I_A = 0$, $I_B = I_C$), e.g. HCN.
- spherical tops ($I_A = I_B = I_C$), e.g. CH₄.
- oblate symmetric tops ($I_A = I_B \leq I_C$), e.g. NH₃.
- prolate symmetric tops ($I_A \leq I_B = I_C$), e.g. CH₃Cl.
- asymmetric tops ($I_A \leq I_B \leq I_C$).

The energy levels for linear-top and spherical-top molecules can be described by using *Equation 2.1.5*, but for symmetric-top rotors, an additional rotational quantum number K needs to be introduced, and the energy levels are:

$$E_{JK} = BJ(J + 1) + (C - B)K^2 \text{ for an oblate top}$$

(*Equation 2.1.7*);

$$E_{JK} = BJ(J + 1) + (A - B)K^2 \text{ for a prolate top}$$

(*Equation 2.1.8*).

Similar to the case in linear top rotors, the rotational constants A , B , and C used in *Equation 2.1.7* and *Equation 2.1.8* are defined as:

$$A = \frac{h^2}{8\pi I_A};$$

$$B = \frac{h^2}{8\pi I_B};$$

$$C = \frac{h^2}{8\pi I_C}$$

(*Equation 2.1.9*).

Most molecules fall into the asymmetric top category. The Schrödinger Equation for the rotation of an asymmetric top molecule can, in general, no longer be solved analytically, and matrix diagonalization techniques are used instead. The rotational wavefunctions are written as linear combinations of symmetric-top wavefunctions. The energy levels for asymmetric-tops can be denoted as $J_{K_a K_c}$ where J is a good quantum number, which corresponds to the total angular momentum, but K_a , K_c are not good quantum numbers, since there is no component of the angular momentum along a molecule fixed axis that is a constant of the motion [14].

2.1.3 Rotational Transitions

A rotational transition is observed only if the molecule itself possesses a permanent electric dipole moment, $\vec{\mu}$. In an asymmetric top molecule, the dipole moment may have components μ_a, μ_b, μ_c along any of the principal inertial axes a, b, c. Rotational transitions can then be labelled according to which dipole moment component drives them as a-, b- or c-type. Additionally, the following selection rules apply:

- for linear molecules: $\Delta J = \pm 1, \Delta M = 0 \text{ or } \pm 1$;
- for symmetric top molecules: $\Delta J = \pm 1, \Delta M = 0 \text{ or } \pm 1, \Delta K = 0$;
- and for asymmetric top molecules: $\Delta J = \pm 1, 0, \Delta M = 0 \text{ or } \pm 1$;
 - for a-type transitions: $\Delta K_a = 0$ and $\Delta K_c = \pm 1$;
 - for b-type transitions $\Delta K_a = \pm 1$ and $\Delta K_c = \pm 1$;
 - for c-type transitions: $\Delta K_a = \pm 1$ and $\Delta K_c = 0$.

Aside from these selection rules, the population difference between the two states is also an important factor that affects the intensity of the transition. A larger population difference results in a larger intensity of a transition. The population of rotational energy levels can be described by a Boltzmann distribution [18], which expresses the population of states as a function of temperature, T , and gives the ratio of populations of two adjacent rotational states, N_{J+1}/N_J , to be:

$$\frac{N_{J+1}}{N_J} = \frac{g_{J+1}}{g_J} \exp \left[-\frac{\Delta E_{rot}}{RT} \right]$$

(Equation 2.1.10).

Here, N_J is the population of the J -th rotational level, ΔE_{rot} is the energy difference between two states, and g_J is the degeneracy of J -th rotational level.

2.1.4 Superposition States

Equation 2.1.1 only describes stationary eigenstates whose probability densities, $\Psi^*\Psi$, are a constant over time. To understand the dynamics of a spectroscopic transition, one has to consider non-stationary states, or superposition states, whose wavefunctions can be represented as linear combinations of wavefunctions of the stationary eigenstates.

Consider an isolated two-level non-degenerate quantum system with stationary states Ψ_1 and Ψ_2 . A superposition state Ψ_s can then be written as follows:

$$\Psi_s(q, t) = c_1(t)\Psi_1(q) + c_2(t)\Psi_2(q)$$

(*Equation 2.1.11*),

where $c_1(t)$ and $c_2(t)$ are the time-dependent probability amplitudes, which are constant in the absence of external radiation. The absolute square of the probability amplitudes, $|c_i|^2$, represents the likelihood of observing the system in its eigenstate Ψ_i , and the sum of all $|c_i|^2$ must be in unity.

Below, the probability density of this superposition state:

$$|\Psi_s|^2 = \Psi_s^*\Psi_s = |c_1|^2|\Psi_1|^2 + |c_2|^2|\Psi_2|^2 + 2\text{Re}\{c_1^*c_2\Psi_1^*\Psi_2\}$$

(*Equation 2.1.12*),

$$\Psi_1^*\Psi_2 = \psi_1^*(q)\psi_2(q)\exp[-i\omega_{21}t], \text{ where } \omega_{21} = \frac{E_2 - E_1}{\hbar}$$

(*Equation 2.1.13*).

From this derivation, it is clear that the probability density, even without the presence of external radiation, has an explicit time-dependence and is oscillating at a steady frequency ω_{21} , which is the transition frequency.

The behavior of the probability density of this superposition state (*Equation 2.1.13*) becomes even more complicated on introducing interactions with a light field and the probability amplitudes

c_i become time-dependent. Instead, c_i are modulated in accordance with the field. The electric field component of externally applied electromagnetic field can be written as:

$$\vec{\varepsilon}(t) = \varepsilon_0 \cos(\vec{k}z - \omega t + \phi)$$

(Equation 2.1.14),

where ε_0 indicates the electric field strength; the wave-vector, \vec{k} , contains information about the wavelength and the direction of propagation, and the frequency and phase of the field are ω and ϕ , respectively. The evolution of the probability density under this light field is defined by two coupled linear differential equations:

$$\begin{cases} \dot{c}_1(t) = -\frac{i}{2}\chi(t) \exp[i\phi] \cdot c_2(t) \\ \dot{c}_2(t) = -\frac{i}{2}\chi(t) \exp[i\phi] \cdot c_1(t) - i(\Delta\omega)c_2(t) \end{cases}$$

(Equation 2.1.15).

Equation 2.1.15 shows a dependency on only two factors, the Rabi frequency, $\chi(t)$, and the detuning, or off-resonance, $\Delta\omega$:

$$\chi(t) = \frac{\vec{u}_{g_{f \leftarrow i}} \cdot \vec{\varepsilon}(t)}{\hbar}$$

(Equation 2.1.16);

$$\Delta\omega = \omega - \omega_{21}$$

(Equation 2.1.17).

Based on Equation 2.1.16, the Rabi frequency is a measure of the strength of the interaction between the molecule and the electric field. It sometimes is referred to as the ‘flip-flop’ frequency because the superposition state evolves from Ψ_1 to Ψ_2 then back to Ψ_1 periodically with the Rabi frequency.

Several important steps have been made in the derivation of *Equation 2.1.15*. These include usage of:

- The electric dipole approximation: the wavelength of transitions between energy levels is much larger than the size of a molecule.
- The rotating wave approximation (RWA) [19]: effects from non-resonant, fast oscillating terms are averaged to zero so that they can be dropped.

2.1.5 Density Matrix Formalism

The theories mentioned in the previous sections only consider a single quantum particle and serve as cornerstones for understanding the properties of an ensemble of particles. Indeed, most spectroscopic experiments do not study just a single particle but many particles, each of which may be prepared in a slightly different way, for example, in a molecular beam experiment. As a result, what really need to be considered is an ensemble average rather than the behavior of the individual particle [20].

Consider an ensemble of N two-state Ψ_a and Ψ_b quantum particles under the influence of an electromagnetic field. Each occupies a unique state, which can be written as:

$$\Psi_N(q, t) = a_N(t)\Psi_a(q) + b_N(t)\Psi_b(q)$$

(*Equation 2.1.18*).

For an arbitrary macroscopic observable of the system, the expectation value, $\langle \hat{O} \rangle$, can be obtained by taking an average over all particles:

$$\langle \hat{O} \rangle = \frac{1}{N} \sum_{i=1}^N \langle \hat{O} \rangle_i = \text{tr} \{ \underline{\rho} \cdot \underline{O} \}$$

(*Equation 2.1.19*),

where \underline{O} is a matrix representation for $\langle \hat{O} \rangle$:

$$\underline{O} = \begin{bmatrix} O_{aa} & O_{ab} \\ O_{ba} & O_{bb} \end{bmatrix} = \begin{bmatrix} \langle a | \hat{O} | a \rangle & \langle a | \hat{O} | b \rangle \\ \langle b | \hat{O} | a \rangle & \langle b | \hat{O} | b \rangle \end{bmatrix}$$

(Equation 2.1.20),

$tr \{ \underline{\rho} \cdot \underline{O} \}$ represents the trace of the $\{ \underline{\rho} \cdot \underline{O} \}$ matrix, and $\underline{\rho}$ is the density matrix that contains all the time-dependent information about the ensemble [21]:

$$\underline{\rho} = \begin{bmatrix} \rho_{aa} & \rho_{ab} \\ \rho_{ba} & \rho_{bb} \end{bmatrix} = \frac{1}{N} \begin{bmatrix} \sum_{i=1}^N a_i a_i^* & \sum_{i=1}^N a_i b_i^* \\ \sum_{i=1}^N b_i a_i^* & \sum_{i=1}^N b_i b_i^* \end{bmatrix}$$

(Equation 2.1.21).

As stated in *Equation 2.1.21*, the diagonal elements of the density matrix are the populations of state Ψ_a or Ψ_b , while the off-diagonal terms are referred to as coherences that describe the phase relation between two eigenstates. The macroscopic polarization \vec{P} , which is an observable is directly related to the experimental signal, is proportional to the coherence terms:

$$\vec{P} = N \cdot \langle \vec{\mu} \rangle = N \cdot \vec{\mu}_{b \leftarrow a} \cdot (\rho_{ab} + \rho_{ba})$$

(Equation 2.1.22).

2.1.6 The Optical Bloch Equations

To understand how coherences are produced requires solving the time-dependent Schrödinger equation of the ensemble. By using the density matrix formalism [22], the time-dependent Schrödinger equation of the system described by *Equation 2.1.18* can then be written as:

$$i\hbar \frac{\partial \underline{\rho}}{\partial t} = [\underline{\hat{H}}, \underline{\rho}] = \underline{\hat{H}}\underline{\rho} - \underline{\rho}\underline{\hat{H}}$$

(*Equation 2.1.23*).

Equation 2.1.23 is also known as the von Neumann equation, where $\underline{\hat{H}}$ is the time-dependent Hamiltonian in the matrix form. Through expansion of *Equation 2.1.23*, the elements of $\underline{\rho}$ are:

$$\begin{cases} \dot{\rho}_{aa} = +i\chi (\rho_{ba} - \rho_{ab}) \cdot \cos(\omega t - \phi_{ab}) \\ \dot{\rho}_{bb} = +i\chi (\rho_{ab} - \rho_{ba}) \cdot \cos(\omega t - \phi_{ab}) \\ \dot{\rho}_{ab} = -i\omega_{ab}\rho_{ab} + i\chi (\rho_{bb} - \rho_{aa}) \cdot \cos(\omega t - \phi_{ab}) \\ \dot{\rho}_{ba} = +i\omega_{ab}\rho_{ba} + i\chi (\rho_{aa} - \rho_{bb}) \cdot \cos(\omega t - \phi_{ab}) \end{cases}$$

(*Equation 2.1.24*).

Similar to the deliberations in *Section 2.1.4.*, these differential equations can be simplified further by transforming the density matrix $\underline{\rho}$ from a laboratory frame into a rotating reference frame $\tilde{\underline{\rho}}$, which rotates with the external radiation field with a frequency ω_{ab} ; then, by applying the rotating wave approximation (RWA) [19], its elements are:

$$\begin{cases} \dot{\tilde{\rho}}_{aa} = +i\chi (\tilde{\rho}_{ba} - \tilde{\rho}_{ab}) \\ \dot{\tilde{\rho}}_{bb} = +i\chi (\tilde{\rho}_{ab} - \tilde{\rho}_{ba}) \\ \dot{\tilde{\rho}}_{ab} = -i\Delta\omega\tilde{\rho}_{ab} + i\chi (\tilde{\rho}_{bb} - \tilde{\rho}_{aa}) \\ \dot{\tilde{\rho}}_{ba} = +i\Delta\omega\tilde{\rho}_{ba} - i\chi (\tilde{\rho}_{bb} - \tilde{\rho}_{aa}) \end{cases}$$

(*Equation 2.1.25*).

Additional rearrangement can be made by introducing the Bloch variables [23, 24]:

$$\begin{cases} s = \tilde{\rho}_{aa} + \tilde{\rho}_{bb} \\ w = \tilde{\rho}_{bb} - \tilde{\rho}_{aa} \\ u = 2\text{Re}\{\tilde{\rho}_{ab}\} = \tilde{\rho}_{ab} + \tilde{\rho}_{ab}^* \\ v = 2\text{Im}\{\tilde{\rho}_{ab}\} = i(\tilde{\rho}_{ab}^* - \tilde{\rho}_{ab}) \end{cases}$$

(Equation 2.1.26),

where s and w indicate the population sum and difference, respectively, while u and v illustrate the coherence, giving the optical Bloch equations [24]:

$$\begin{cases} \dot{u}(t) = -\Delta\omega(t) \cdot v(t) \\ \dot{v}(t) = +\Delta\omega(t) \cdot u(t) - \chi(t) \cdot w(t) \\ \dot{w}(t) = +\chi(t) \cdot v(t) \end{cases}$$

(Equation 2.1.27).

The optical Bloch equations explain the dynamics of a two-state system interacting with a classic electromagnetic mode as long as the weak-field and the near-resonance conditions are valid (see *Section 2.1.4*). For most cases in rotational spectroscopy, only one transition can resonate with the incoming microwave pulse in a given fraction of time. For this reason, it can be treated as a two-state problem, known as the two-state approximation, and can be solved by using the optical Bloch equations. With the optical Bloch equations, the macroscopic polarization originally given by *Equation 2.1.22* can be redefined as:

$$\vec{P} = N \cdot \vec{\mu}_{b \leftarrow a} \cdot (u(t) \cos(\omega t) - v(t) \sin(\omega t))$$

(Equation 2.1.28).

In the derivation of the Bloch equations, relaxation terms are neglected, which are responsible for the decay of the molecular emission signal. Phenomenological relaxation terms can be introduced in *Equation 2.1.27* to account for the decrease in signal over time.

2.1.7 Solution of The Bloch Equations

To understand the origin of the molecular signal, it is instructive to solve the Bloch equations, first for the molecular system being in the presence and then in absence of an external field.

(a) Excitation Pulse: ON

To solve the Bloch equations analytically, it can be assumed that the excitation power is high, such that the off-resonance term $\Delta\omega(t)$ is small compared to the Rabi frequency; i.e. $\Delta\omega(t) \ll \chi(t)$. In the following, $\Delta\omega(t)$ will be neglected, and the Bloch equations (*Equation 2.1.27*) are simplified:

$$\begin{cases} \dot{u}(t) = 0 \\ \dot{v}(t) = -\chi(t) \cdot w(t) \\ \dot{w}(t) = +\chi(t) \cdot v(t) \end{cases}$$

(Equation 2.1.29)

By choosing the initial condition as $u_{t=0} = v_{t=0} = 0$ and $w_{t=0} = w_0$, the following results:

$$\begin{cases} u(t) = 0 \\ v(t) = -w_0 \sin(\chi \cdot t) \\ w(t) = +w_0 \cos(\chi \cdot t) \end{cases}$$

(Equation 2.1.30)

This indicates that the coherence term v oscillates with the Rabi frequency during the excitation pulse.

In the above equation, if $\chi \cdot t = \pi/2$, termed a $\pi/2$ pulse, or an odd-numbered multiple thereof, the system has reached the greatest absolute coherence, $v_{t_{\pi/2}} = -w_0$, and the population difference $w_{t_{\pi/2}} = 0$. This is shown in the Bloch sphere diagram [21] in Figure 2.1.1. (a). On the other hand, if $\chi \cdot t = \pi$, named a π pulse, a population inversion or a return to the initial conditions is observed, depending if it is an odd-numbered or even-numbered multiple of π (see Figure 2.1.1. (b)). After such an $n \pi$ pulse, the coherence terms are zero.

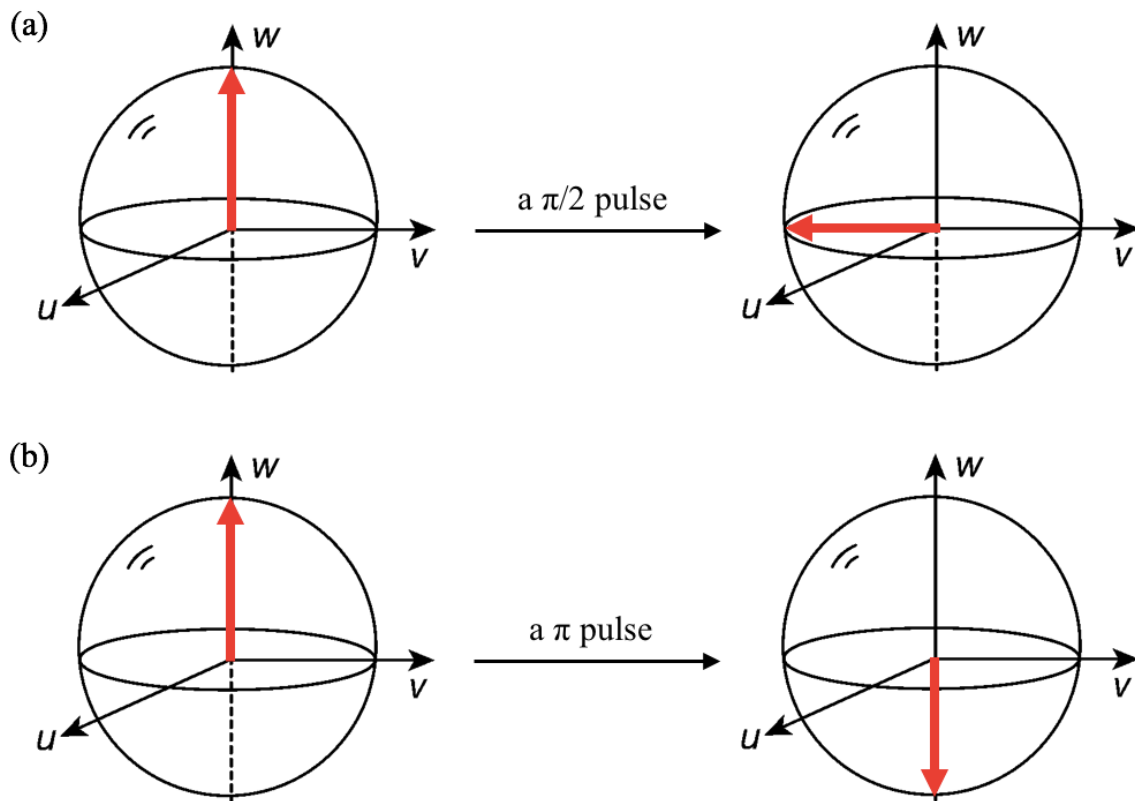


Figure 2.1.1 Time evolution of the system in the presence of an external electromagnetic field; (a) a resonant $\pi/2$ pulse, and (b) a resonant π pulse.

(a) Excitation Pulse: OFF

In the absence of an external field, $\chi(t) = 0$, and, in general, $\Delta\omega(t) \neq 0$; therefore, the optical Bloch equations (*Equation 2.1.27*) are simplified:

$$\begin{cases} \dot{u}(t) = -\Delta\omega(t) \cdot v(t) \\ \dot{v}(t) = +\Delta\omega(t) \cdot u(t) \\ \dot{w}(t) = 0 \end{cases}$$

(*Equation 2.1.31*).

An analytical solution for *Equation 2.1.31* is obtained by using the conditions after a $\pi/2$ pulse as boundary conditions, i.e. $u_{t_{\pi/2}} = 0$, $v_{t_{\pi/2}} = -w_0$ and $w_{t_{\pi/2}} = 0$:

$$\begin{cases} u(t) = +w_0 \sin(\Delta\omega \cdot t) \\ v(t) = -w_0 \cos(\Delta\omega \cdot t) \\ w(t) = 0 \end{cases}$$

(*Equation 2.1.32*)

The coherence of the system is oscillating between u and v components at the off-resonance frequency, as indicated in *Figure 2.1.2*.

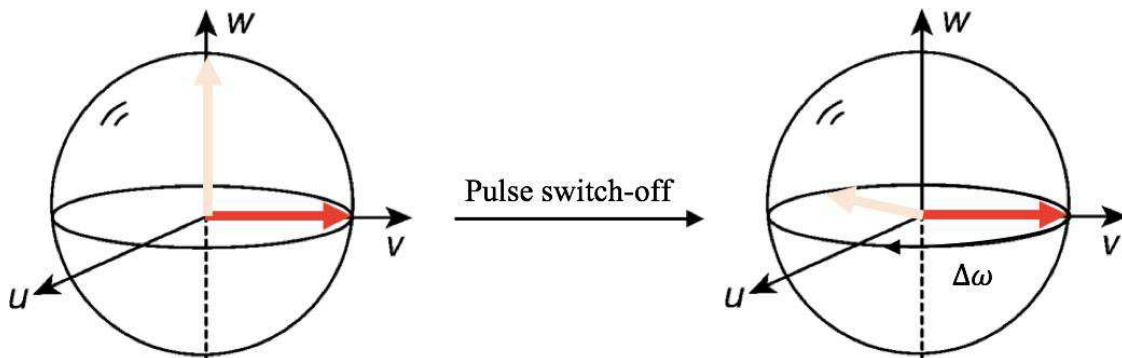


Figure 2.1.2 The coherence of system is oscillating between u and v components at the off-resonance frequency $\Delta\omega$.

2.2 Supersonic Jet Expansion

The energy gap between rotational energy levels is generally far smaller than that between vibrational energy levels, resulting in a broad population distribution at room temperature where relatively high- J rotational states are predominant, at least for molecules with five or six atoms or more. This makes microwave experiments at room temperature especially challenging because a large number of rotational transitions are available, but with low intensities because of the small population differences (see *Equation 2.1.10* and *Equation 2.1.22*). This results in complicated rotational spectra that are hard to assign. Therefore, a narrower population distribution is required to simplify the spectra, which means that one must find a way to cool down the molecular sample.

Among different cooling techniques, the supersonic jet expansion, first introduced by Kantrowitz and Gray in 1951 [25], has been used widely in molecular beam experiments and in rotational spectroscopy. In a supersonic jet expansion, a gas mixture is expanded adiabatically through an, often pulsed, nozzle into a vacuum chamber, which is kept at pressure of about 10^{-6} to 10^{-7} Torr. The diameter of the nozzle orifice is selected carefully so that it is much larger than the mean free path of the gas. Once the nozzle is opened, typically for a time between 500 to 800 μs , many collisions will occur near the orifice, beginning to equalize the molecular velocities and leading to the formation of molecular complexes and clusters. Only those molecules moving in the direction of the exit can expand into the chamber, leading to a relatively narrow velocity distribution of the flow. Once the gas leaves the high-density region, it remains in a collision-free environment during the rest of the experiment. This environment is essential for stabilizing the isolated, cold, and gaseous molecules and molecular clusters at temperatures that are well below their condensation point in the bulk, as illustrated in *Figure 2.2.1*.

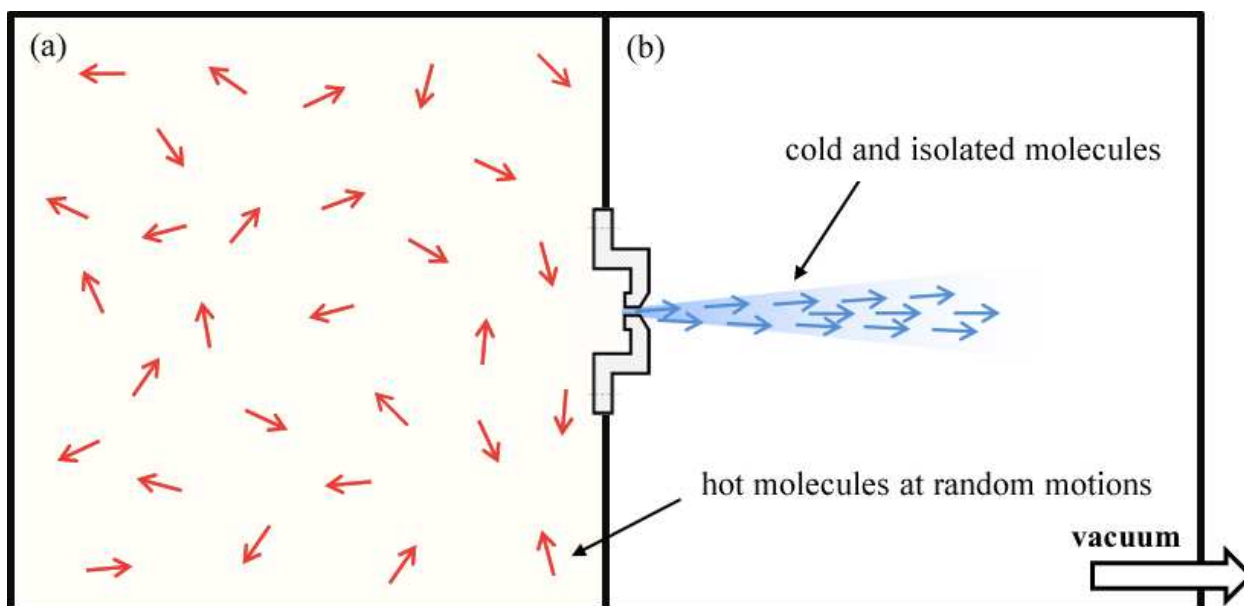


Figure 2.2.1 An illustration of a supersonic jet expansion.

(a) A gas cylinder contains the sample gas at pressure of about 1 to 3 bars at room temperature.

(b) The vacuum chamber at a pressure of about 10^{-6} to 10^{-7} Torr. The molecules cool to a rotational temperature of about 2 K.

Typically, molecules of interest are seeded into a noble backing gas, such as He, or Ne, for the supersonic jet expansion. Noble gases have no rotational or vibrational degrees of freedom that need to be cooled and achieve very low translational temperatures (< 1 K) that, in turn, helps to cool the seeded molecules through collisions. The time frame of collisions is not long enough to establish equilibrium, and translational, rotational, and vibrational temperatures are in the ranges of \sim mK, < 2 K, 50 K to source temperature, respectively, depending on the energy gaps. The low rotational temperature of a few K results in spectra that are less congested than at room temperature.

2.3 Microwave Spectrometers

Early microwave studies trace back to the 1940s and utilized the Stark modulation technique [26, 27], where a waveguide sample cell was used, and a modulated electric field was applied. Since then, many scientists have striven to design more powerful instruments for studying molecular rotational spectra. In order to study the structures of weakly bonded complexes, Balle and Flygare took advantage of the supersonic jet expansion (see *Section 2.2*) with a pulsed-nozzle and replaced the waveguide sample cell by a cavity, a so-called Fabry–Pérot resonator, in 1981 [28]; this is now known as a Balle–Flygare type or cavity-based Fourier-transform microwave (FTMW) spectrometer [29-31]. Although the cavity-based instrument can achieve extraordinary sensitivity and resolution due to the use of a resonator, only a narrow bandwidth, about 1 MHz, can be investigated at a time. Later in 2006, the Pate group published their design of the broadband, several GHz, chirped-pulse spectrometer [32] that is based on the modern success of ultrafast electronics, especially the arbitrary waveform generator (AWG) [33]. Both designs have their advantages: the chirped pulse instrument has a large bandwidth and the cavity type has a high spectral resolution. Details of the cavity-based and the chirped-pulse FTMW spectrometers used for this work are listed in the following sections.

2.3.1 The Cavity-based FTMW Spectrometer

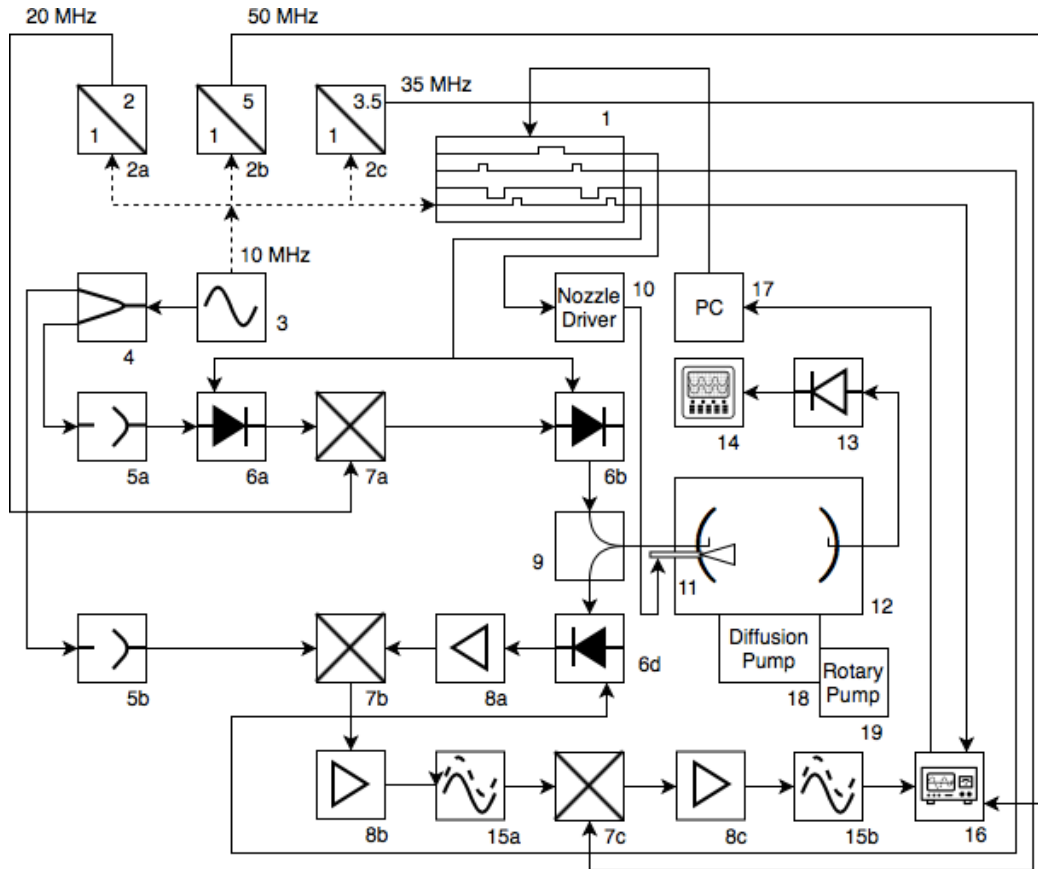


Figure 2.3.1 A schematic diagram of the revised Balle–Flygare type FTMW spectrometer.

Components are denoted by numbers: ① pulse generator, ② frequency multipliers, ③ microwave synthesizer, ④ power divider, ⑤ isolators, ⑥ PIN diode switches, ⑦ mixers, ⑧ amplifiers, ⑨ circulator, ⑩ nozzle driver ⑪ nozzle, ⑫ microwave cavity with a Fabry–Pérot resonator, ⑬ Schottky diode detector, ⑭ oscilloscope, ⑮ narrow-band bandpass filter, ⑯ analog-to-digital converter and transient recorder, ⑰ personal computer, ⑱ diffusion pump, ⑲ mechanical pump

The blueprint of the cavity-based FTMW spectrometer used in this thesis has been improved from the original Balle–Flygare design [34-36]. Changes include the orientation of the pulsed-nozzle parallel to the axis of the Fabry–Pérot resonator to yield a coaxial propagation of the molecular beam with the microwave radiation. This induces a Doppler splitting in each transition, along with 10-fold decrease in the linewidth [37, 38] resulted from a longer path to interact with the incident radiation. As a result, the resolution is enhanced significantly. Moreover, an automatic step-scan capability has been implemented [39], making searching for unknown transitions over larger frequency ranges an easier task. For this cavity-based instrument, the frequency uncertainty is ~ 2 kHz and the full linewidth at half height is ~ 10 kHz. A schematic diagram of this spectrometer is given in *Figure 2.3.1*, and descriptions for the main components are provided.

A. Microwave cavity

The core of this instrument is a Fabry–Pérot resonator, which accumulates energy by generating a standing wave of the incident microwave radiation. This cavity resonator consists of two spherical aluminum mirrors (260 mm diameter, 380 mm radius of curvature) and serves as the sample cell. One of the mirrors is mounted into one of the flanges of the vacuum chamber. The second mirror is mounted inside the vacuum chamber and is moveable so that the mirror separation can be tuned (from 200 to 400 mm) into resonance with the external microwave radiation. The incident microwave-pulse is coupled into and out of the resonator through the center of the fixed mirror via an L-shaped antenna. A second antenna is mounted into the moveable mirror and used to monitor the cavity response for tuning. A 12-inch diffusion pump (Edwards, Diffstak 250; ⑱), with a pumping speed of 2,000 L/s, supported by a mechanical pump (Edwards, E2M40; ⑲) is used to maintain a pressure of less than 10^{-4} Torr during pulsed nozzle operation. The frequency range of this instrument is from 2.5 to 26 GHz.

An important specification of the cavity is the quality factor, Q . The Q -factor is defined as the ratio of the total stored electromagnetic energy to the power dissipation, and can be defined as:

$$Q = \frac{\text{resonant frequency}}{\text{frequency bandwidth}}$$

(Equation 2.3.1).

The Q -factor for this instrument is somewhat frequency dependent and is on the order of 10^4 . That means that, for a 10 GHz incident pulse, the cavity bandwidth is about 1 MHz.

B. Excitation pulse

The excitation pulse is generated from the output of a continuous-wave microwave synthesizer (HP 83711A, ③). After the synthesizer, the microwave radiation is divided by a power divider (④) into two arms, the detection and excitation arm. The microwave signal at frequency ν_0 goes into a PIN diode switch (⑥a) to form the excitation pulse, which is typically several μs in length, and is then mixed with a 20 MHz signal to create two sidebands ($\nu_0 \pm 20 \text{ MHz}$) in a double balanced mixer (⑦a). The output signal from the mixer passes through a power amplifier (⑧a) and through the second PIN diode switch before it is propagated into the cavity via a circulator (⑨). With a pulse power of a few mW and the Q -factor mentioned above, field strengths of $\sim 180 \text{ V/m}$ inside the cavity can be attained [30, 31].

C. Detection arm

Due to the weakness of the emitted molecular signal ($\sim 10^{-3}$ V/m [40]), a double superheterodyne detection scheme is applied. The output signal from the cavity can be written as $\nu_0 + 20 \text{ MHz} + \Delta\nu_m$, where $\Delta\nu_m$ is the off-resonance of the weak molecular emission signal. This signal is captured by the antenna and coupled back to the detection arm of the circuit via the circulator (⑨). An additional PIN diode switch (⑥d) is situated right after the circulator to protect the detection system from the excitation pulse. The signal is amplified (⑧b), mixed with the original microwave radiation (ν_0) in an image rejection mixer (⑦b), and down-converted to $20 \text{ MHz} + \Delta\nu_m$. After a narrow-band bandpass filter (⑬), additional down-conversion to $15 \text{ MHz} + \Delta\nu_m$ is done by a radio frequency mixer (⑦c). After the last amplification of the signal (⑧a), the signal is then filtered once more through a bandpass filter. A computer-based analog-to-digital converter and transient recorder board (8-bit A/D-converter, 50 MHz sampling interval, 32 k on-board memory; ⑩) is used for analog-to-digital conversion and sampling of the final time-domain signal. Finally, background subtraction, signal averaging, and Fourier transformation are processed by a personal computer to give a frequency power spectrum.

D. Pulse sequence



Figure 2.3.2 A typical pulse sequence programmed in the cavity-based FTMW spectrometer.

A highly stable transistor-transistor logic (TTL) pulse sequence to control microwave pulse generation and data acquisition, as shown in *Figure 2.3.2*, is important to the experiment to ensure phase coherent averaging of the molecular emission signal: (a) a 400-to-900- μs -long molecular pulse is fired only in every second cycle to allow for background subtraction; (b) the PIN diode switches in the excitation arm are set to low insertion loss for about 1 μs to produce the excitation pulse; (c) meanwhile, PIN diode switch in the detection arm blocks the microwave-pulse from the sensitive detection electronics; (d) after a long enough delay time, about 10 to 25 μs after the end of microwave-pulse, the data acquisition of the molecular signal is triggered.

2.3.2 The Chirped-pulse FTMW Spectrometer

As highlighted previously, the traditional cavity-based FTMW spectrometer has a high sensitivity and resolution advantage, but a pronounced time-consuming disadvantage. Even with the capability of the automatic step-scan, a 100 MHz measurement easily can take over 12 hours to be completed. Therefore, the use of a broadband chirped-pulse FTMW spectrometer is necessary. The instrument used in this thesis has ~ 25 kHz resolution [41] and a schematic diagram is shown in *Figure 2.3.3*.

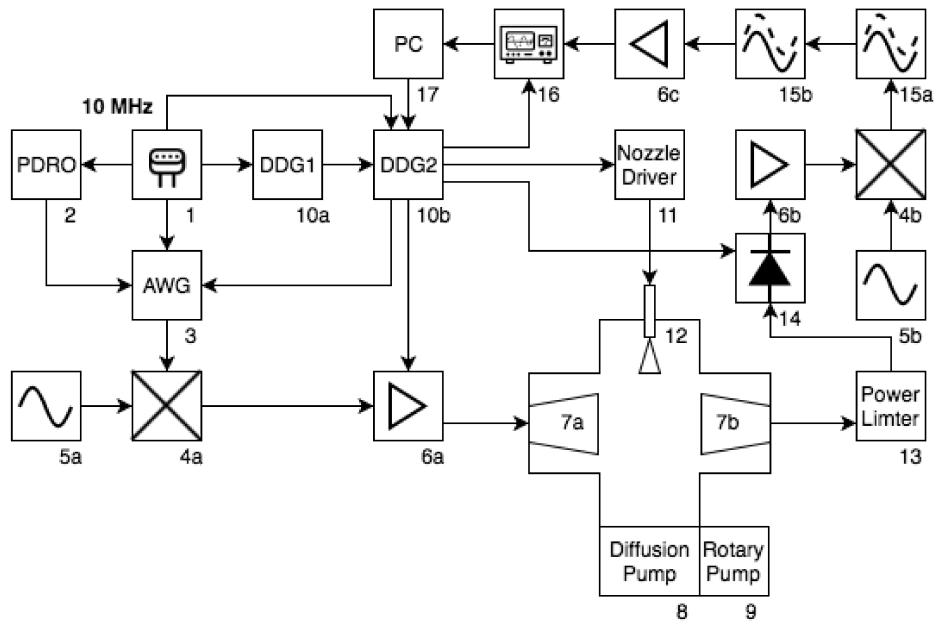


Figure 2.3.3 A schematic diagram of the chirped-pulse FTMW spectrometer.

Components are denoted by numbers: [1] 10 MHz rubidium frequency standard, [2] 3.96 GHz phase-locked dielectric resonator oscillator (PDRO), [3] arbitrary waveform generator (AWG), [4] mixers, [5] microwave synthesizers, [6] amplifiers, [7] horn antennas, [8] diffusion pump, [9] rotary pump, [10] digital delay generators (DDG), [11] nozzle driver, [12] nozzle, [13] power limiter, [14] PIN diode switch, [15] low pass filters, [16] fast-digital storage oscilloscope, [17] personal computer.

A. Sample chamber

A set of two wide-band and high-gain MW horn antennas (RF/Microwave Instrumentation, ATH7G18; [7]), facing each other at a separation of 300 mm, are mounted inside a six way-cross vacuum chamber. Molecules are introduced into the chamber as a supersonic jet expansion (see Section 2.2) through a pulsed-nozzle (General Valve, Series 9; [12]) moving perpendicularly to the microwave propagation direction between the horn antennas, so that no Doppler splitting is observed. The vacuum chamber is pumped by a 1,300 L/s diffusion pump (Edwards, Diffstak 160; [8]), supported by a rotary-vane mechanical pump (Edwards, E2M30; [9]). To help eliminate artefacts resulting from reflections of microwaves, the inside of the vacuum chamber is lined with tiles of microwave-absorbing foam.

B. Chirped-pulse

A chirped-pulse is a frequency sweep over certain range during a given duration of the pulse, which can be synthesized easily by an arbitrary wave generator (AWG; Tektronix, AWG710B; [3]). The AWG is referenced to an external 3.96 GHz signal, generated by a phase-locked dielectric resonator oscillator (PDRO; [2]). AWG and PDRO are referenced to a 10 MHz frequency standard (Stanford Research Systems, FS725; [1]) to ensure phase coherent averaging of the molecular emission signal. In a standard experiment, the AWG produces a 4 μ s chirped-pulse with a frequency range $\Delta\nu_{cp}$ of 1 GHz, between ~ 0 and 1 GHz.

The chirped-pulse from the AWG is mixed with a fixed frequency, ν_0 , from a microwave synthesizer (Agilent Technologies, E8257D; [5a]) and up-converted via a double balanced mixer ([4a]) to a 2-GHz bandwidth chirped-pulse, $\nu_0 \pm \Delta\nu_{cp}$, centered at the given microwave frequency ν_0 . The operational window of this instrument is 8 to 18 GHz, and the center frequency can be set to cover the specific frequency region of interest. Unlike in the cavity-based instrument, where a resonator accumulates the energy, it is essential to equip the chirped pulse instrument with a powerful amplifier to induce enough molecular polarization to produce the signal. Therefore, after the up-conversion, the chirped-pulse is amplified by a 20 W solid-state amplifier (Microwave Power, L0818-43; [6a]) before being broadcast into the chamber by one of the horn antennas.

C. Detection system

In a chirped pulse experiment, the excitation pulse is swept very fast (500 MHz/ μ s) through a rotational resonance. In such a ‘fast passage’ experiment [42], the concept of a $\pi/2$ excitation pulse no longer applies, but the set of optical Bloch equations (*Equation 2.1.27*), can still be used to describe the generation of a coherent molecular emission signal. In this chirped-pulse FTMW spectrometer, the broadband fast passage emission signal of molecules is detected by a superheterodyne detection method.

The detection system includes a power limiter (high-power PIN diode; [13]) and a PIN diode switch ([14]) that protect the low-noise amplifier ([6b]) from the high-power chirped-pulse. After amplification, the emission signal is heterodyned by another double balanced mixer ([4b]) with another fixed microwave frequency that is 1.5 GHz higher than the center frequency of the chirp ($\nu_0 + 1.5$ GHz) in order to prevent folding of the rotational spectrum. Next, a 4.4 GHz low-pass filter is deployed to filter out any high frequency artifacts after the mixing. The final signal is

detected and averaged by a fast-digital storage oscilloscope (Tektronix, TDS6124C; [16]) in the time domain. The digitization rate of this oscilloscope is 40 GS/s with 8-bit vertical resolution. The oscilloscope is also phase-locked by the same 10 MHz reference signal to ensure phase synchronous averaging of emission signals. Finally, the time domain signal is background subtracted, averaged, and Fourier transformed into the frequency domain by a personal computer. For each molecular pulse, eight measurements are done to provide further averaging.

D. Time sequence

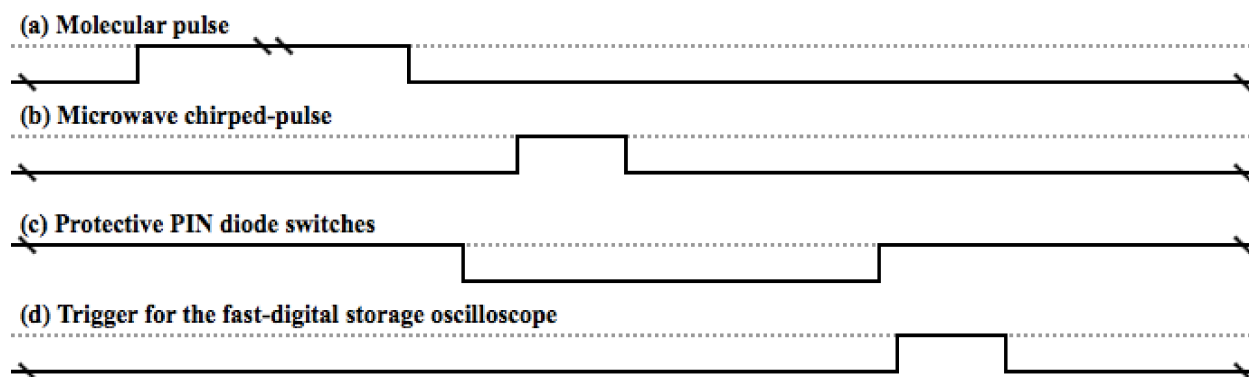


Figure 2.3.4 A typical time sequence to control the chirped-pulse FTMW spectrometer.

For acquiring high quality chirped-pulse rotational spectra, a proper time sequence is crucial. Because phase stability is essential in this instrument, all devices are referenced to a 10 MHz rubidium frequency standard ([1]). A digital delay generator (DDG; [10]) produces a TTL pulse train to control a single experiment; the timing between individual measurement cycles is controlled by another DDG to prevent signals from overlapping. An example of a time sequence for the (a) molecular pulse, (b) microwave chirped-pulse, (c) protective PIN switch, and (d) oscilloscope trigger is shown in *Figure 2.3.4*. A delay (100 to 200 μ s) is added right before the initiation of a chirped-pulse to ensure that the gas expansion from a supersonic-jet can reach the active region between the two horn antennas.

2.4 Theoretical Calculations

Nowadays, along with evolutions and innovations in modern technology and computer science, theoretical calculations play a much greater role than ever before in chemistry. In rotational spectroscopy, many scientists now use computational approaches to predict molecular structures to aid in the spectroscopic assignment process, especially in studying hydrogen-bonded complexes or weakly-bonded van der Waals clusters. Often, several conformers with different energies exist, and it is possible to identify the global minimum structure, relative energies and barriers among different local minima, for example. Typically, a microwave experiment is guided by a predicted spectrum that is simulated from the theoretical rotational constants (A, B, and C) and other parameters. In addition to the initiation of a research project, many pivotal insights are gained by using theoretical calculations to analyze the experimental results. The following sections are brief introductions of the available computational methods used in the study of the hydrogen peroxide – formic acid complex (see *Chapter 3*).

2.4.1 *Ab initio* Wavefunction Calculations

Ab initio is a Latin term meaning ‘from the beginning’ or, conventionally, ‘from first principles of quantum mechanics’ in physics and chemistry, implying that physical constants are the only inputs for the calculation. The first *ab initio* calculation in a computational chemistry study was introduced by D. P. Craig and I. G. Ross in 1950 [43]. After much effort by numerous scientists over several years, *ab initio* calculations can provide quite accurate structural and energetic information about small to medium-sized molecules (up to about 25 atoms).

Several *ab initio* methods have been developed over the decades, such as Hartree–Fock (HF) [44], Møller–Plesset perturbation theory [45], configuration interaction [46], or other multi-reference methods. Among the post-HF methods, the Møller–Plesset perturbation theory, also known as many-body perturbation theory, is a relatively economical method for studying small systems, especially those associated with hydrogen bonding, with good accuracy [47, 48]. This method uses perturbation theory to account for the electron correlation effects to the second (MP2), to the third (MP3), and higher orders (MP n). The MP2 method usually outperforms the others since other higher orders of theory seem to overcorrect the electron correlations.

The choice of basis set can influence dramatically the computational time and the result for a given method. Often, Pople’s split-valence basis set [49], such as the 6-311++G(2d,p) basis set, is used, where several auxiliary functions help to improve the performance. These include polarization functions, denoted by * or (d,p), and diffuse functions, marked by +, which are important to capture the details of the hydrogen bonding.

2.4.2 *Ab initio* Density Functional Theory

Density functional theory is also a widely used approach. Using this theory, the properties of a system can be determined by functionals that describe the spatially dependent electron density [50]. The computational cost is much lower compared to wavefunction approaches. A drawback of density functional theory is that the result cannot be systematically improved by higher levels of theory or larger basis sets. One of most widely used functionals is the B3LYP method [51], which is a hybrid functional where the exchange energy is combined with the exact energy calculated by the HF method. It has been applied also in the present work for speeding up the searching process of possible geometries of the complex (see *Section 3.2*).

2.5 Scientific Software

Several scientific programs were used for multiple purposes throughout the work for this thesis (see *Chapter 3*); some information is listed in this section for reference.

(a) Theoretical calculations

Both high-level *ab initio* wavefunction and DFT calculations were carried out for searching and optimizing geometries via the commercial Gaussian09 program package [52] (see *Section 3.2*). For the wavefunction-based calculations the MP2 method with the 6-311++G(2d,p) Pople basis set [45, 49] was used, and the density-based calculations were accomplished with the B3LYP functional [51] and the 6-31G(d,p) basis set. Several intrinsic reaction coordinate (IRC) calculations were also carried out via this program by using ‘irc=(calcall, maxpoints=2000) mp2/6-311++g(2d,p) scf=verytight’ keywords in the input files (see *Section 3.5*).

(b) Spectral prediction and fitting programs

Spectrum simulations or predictions were done using the PGOPHER (version 10.0.505) program [53] with its user-friendly graphical user interface (GUI) and many customizable physical parameters, such as the temperature or centrifugal constants. The final fits were done with Pickett’s SPFIT program [54] (see *Section 3.6*).

(c) Electron density topology analyses

The topology of the molecular electron density was analyzed (see *Section 3.7*) using the Quantum Theory of Atoms in Molecules (QTAIM) [55, 56] and Non-Covalent Interactions (NCI) [57] approaches, as implemented in the Multiwfn (version 3.4.1) [58] and Visual Molecular Dynamics (VMD, version 1.9.3) programs [59].

CHAPTER 3

A Study of the Hydrogen Peroxide – Formic Acid Complex

3.1 Introduction

How a molecule interacts with other molecules is an interesting and important topic for scientists; it leads to many questions that can be asked and answered, such as the mechanism of chemical reactions, the aggregation process of particles or aerosols in the atmosphere, and even the design of novel materials or medical treatments to improve the quality of life.

3.1.1 Hydrogen Peroxide and its Significance

Hydrogen peroxide (H_2O_2) is particularly interesting in the context of intermolecular interactions because all of its constituent atoms can potentially be involved in hydrogen bonding interactions and because it plays a role in a number of processes of biological, atmospheric, and geological significance, for example. In biological systems, hydrogen peroxide not only exhibits cytotoxic effects [60], but many living organisms also exploit its reactivity in mechanisms such as message signal sensing [61], oxidative biosynthesis, or in host defense [62]. Hydrogen peroxide is also interesting in a chiral recognition context because of the possibility to serve as a prototype for chiral recognition events [63, 64]. On the other hand, scientists have detected hydrogen peroxide on the surface of Mars [65], where a thick, up to 200 m, layer of oxides has been detected. Researchers have found that the spatial distribution of hydrogen peroxide is a function of the seasonal cycle in Mars [66], and studies have suggested that hydrogen peroxide plays a key role in the oxidation of the Martian surface [67, 68]. Hydrogen peroxide is also known to be one of the most significant oxidants in Earth's atmosphere [69]. There are multiple pathways for hydrogen peroxide formation in both the gas and aqueous phases [69, 70], mostly through a process of hydroxyl radical recombination [71]. The concentration of hydrogen peroxide in the atmosphere is a few ppbv (parts per billion by volume) [69-72] and is sensitive to the presence of pollutants

such as SO₂, NO₂, etc. [73], with a lifetime of a few hours [74]. Hydrogen peroxide is being used to monitor air pollution [72] and to evaluate the oxidative capacity of the atmosphere [68, 75]. Furthermore, environmental studies have shown that hydrogen peroxide is involved in the formation of acid rain [76, 77], regulation of the atmospheric concentration of ozone [78], and in pathways to generate various secondary organic aerosols (SOAs) [79-81] through photo-oxidation processes, indicating that hydrogen peroxide also can influence the air quality [82].

Hydrogen peroxide is a non-planar molecule with an H–O–O–H dihedral angle of 111.5° in the isolated molecule. This makes hydrogen peroxide a transiently chiral molecule, and it can interconvert between enantiomers through torsional motions of the OH groups. Its structure and internal dynamics have fascinated many spectroscopists and spectroscopic studies of hydrogen peroxide began in the 1930s [83]. The first microwave spectra of hydrogen peroxide were recorded by Massey and Bianco [84] and subsequently by Hunt *et al.* studied its spectrum in the far-infrared region [85]. This was followed by the work of Helminger and co-workers in the late 1980s. They thoroughly studied the extraordinary complexity of the spectrum of hydrogen peroxide using rotational spectroscopy, where tunneling barriers of 387 and 2,563 cm⁻¹ were determined for the *trans-to-trans* (C_{2h} transition state) and *trans-to-cis* (C_{2v} transition state) torsional motions, respectively [86, 87]. Due to the tendency of hydrogen peroxide to decompose and because of the complexity of the torsional tunneling motions, there are few experimental studies of complexes involving hydrogen peroxide, which are limited to the matrix isolation technique [88-102]. Gas-phase spectra of complexes with hydrogen peroxide as a subunit have thus far not been observed.

3.1.2 An Appropriate Choice for the Study

The aim of the present work is to study the intermolecular interactions of hydrogen peroxide with another molecule. The experimental approach is to form a binary complex involving hydrogen peroxide, and to study this complex using high-resolution rotational spectroscopy. In order to make the assignments and analyses of the spectrum manageable, it was desirable to select a binding partner which could quench the torsional tunneling motions of the hydrogen peroxide subunit. Ideally, the partner molecule would ‘hold’ one or two hydroxyl groups of hydrogen peroxide tightly, for example through hydrogen bonding.

Formic acid was selected as a promising partner molecule for several reasons, namely the simplicity of its structure, its high vapor pressure, and several readily available sites for hydrogen bonding. Formic acid is the smallest carboxylic acid and plays an important role in many chemical fields, for example in atmospheric chemistry [103-107]. In the atmosphere, the source of formic acid can be varied but is primarily due to forest emissions [105-107], which are a main cause of rainfall acidity in remote regions [108]. Aside from its environmental importance, formic acid is also a prototypical molecule for the study of intermolecular interactions, especially hydrogen bonding [109-112]. Formic acid can be both a donor or an acceptor in the formation of hydrogen bonding, and sometimes the hydrogen bonds can be even stronger than those involving water [113, 114]. Based on these facts, it was anticipated that formic acid can limit the torsional motions of hydrogen peroxide by establishing two strong hydrogen bonds, forming a cyclic structure that has been found in similar systems [112, 113, 118].

3.2 Conformational Searches

Before carrying out experiments in the laboratory, possible conformers for the hydrogen peroxide – formic acid complex were searched theoretically. Throughout the search process, DFT calculations, using the B3LYP functional with the 6-31G(d,p) basis set, were used at the beginning, while more accurate geometry optimizations were done at the MP2/6-311++G(2d,p) level of theory (see *Section 2.4*). With no imaginary frequencies found in the frequency analyses, all optimized structures reported in this thesis are verified to be the true energy minima. Zero-point energy (ZPE) corrections were also determined from these analyses. By using Boys and Bernardi's counterpoise correction method [115], the basis set superposition error (BSSE) was considered and corrected for in all found structures.

In the conformational search strategy, the *cis-trans* isomerism of formic acid was considered first. A 16.3 kJ•mol⁻¹ energy difference between ground state *trans*- and *cis*-formic acid monomers was reported in previous work [116]; therefore, it was anticipated that the most stable conformer of the complex would contain a *trans*-formic acid subunit. To find the global minimum of the complex, all possible arrangements must be examined carefully. There are 4 distinct positions for placing the hydrogen peroxide into 2 isomers of the formic acid, including 3 possible orientations on the molecular plane, and 1 set of equivalent positions at the top or bottom of that plane. The orientation of hydrogen peroxide with respect to the heavy atom plane of formic acid gives further possible configurations. In the *ab initio* calculations six conformers were found and their optimized structures are shown in *Figure 3.2.1*. Only the first two structures were chosen to be experimental candidates since the others are too high in energy to be abundant enough in the molecular expansion. These two are 7- and 6-membered ring-like structures as the global and the first local minimum, labeled as HP-FA-I and HP-FA-II, respectively; their calculated spectroscopic constants and their relative energies are listed in *Table 3.2.1*.

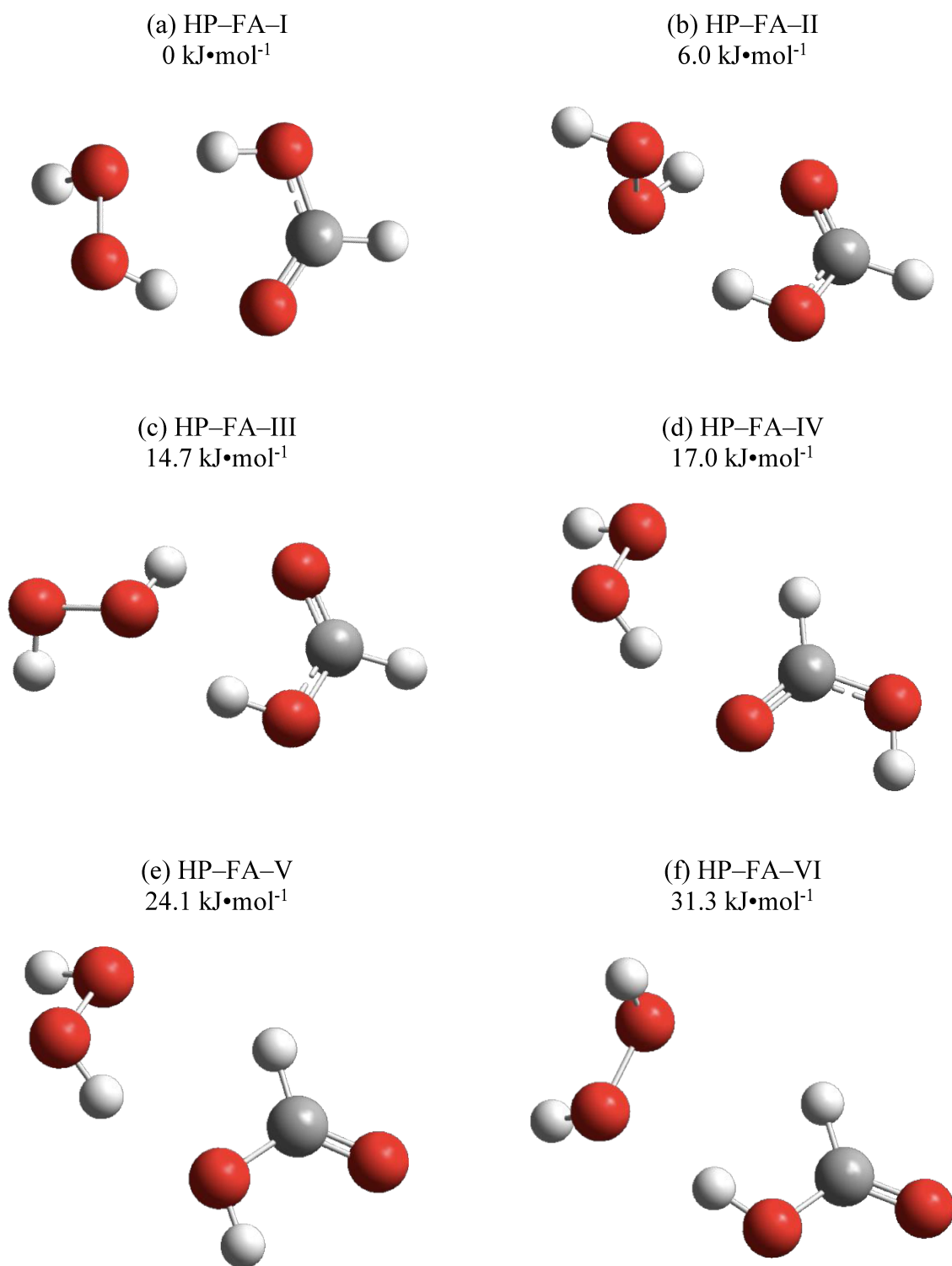
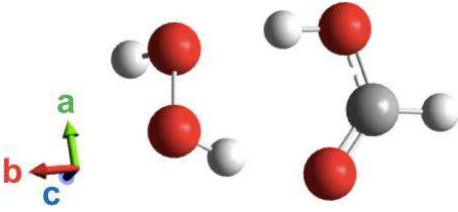
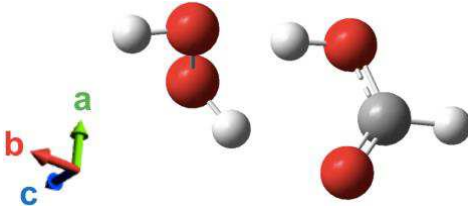


Figure 3.2.1 Six optimized structures of the HP-FA complex and their relative energies.

All structures and energies were calculated at the MP2/6-311++G(2d,p) level of theory. The energies given are relative to that of the lowest energy conformer, HP-FA-I.

Table 3.2.1 Calculated spectroscopic constants for the lowest two HP-FA conformers

	HP-FA-I		HP-FA-II	
				
	B3LYP/ 6-31G(d,p)	MP2/ 6-311++g(2d,p)	B3LYP/ 6-31G(d,p)	MP2/ 6-311++g(2d,p)
E /kJ•mol ⁻¹	0	0	6.6	6.0
A /MHz	8223	8216	9275	9075
B /MHz	2991	2949	2487	2473
C /MHz	2214	2213	2156	2153
$ \mu_a $ /D	0.84	1.25	0.69	0.44
$ \mu_b $ /D	1.40	1.24	0.09	0.11
$ \mu_c $ /D	1.58	1.61	0.26	0.12

3.3 Sample Preparation

Gaseous mixtures containing 0.2% formic acid (95% purity, Sigma Aldrich) were prepared at 2.5 bar without further purification using two different backing gases. For a measurement with the best signal-to-noise ratio, the backing gas was chosen to be helium for the chirped-pulse and neon for the cavity-based experiments. A photo of the cavity-based FTMW spectrometer is presented in *Figure 3.3.1*. Because pure hydrogen peroxide decomposes easily, it was not pre-mixed within the gaseous mixtures. Instead, a urea – hydrogen peroxide adduct ($\geq 97\%$ purity, Sigma Aldrich) was used as the source of pure hydrogen peroxide [89]. The solid sample was placed inside the stainless-steel nozzle cap, as illustrated in *Figure 3.3.2*.

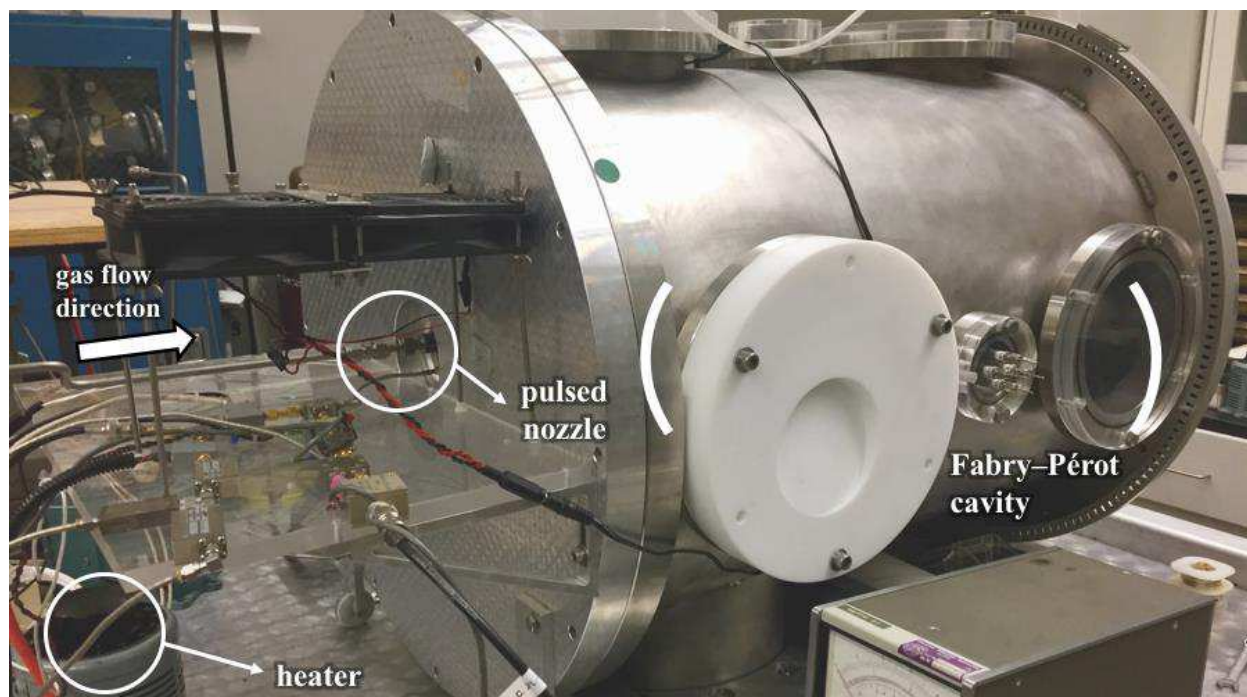


Figure 3.3.1 A photo of the cavity-based FTMW spectrometer.

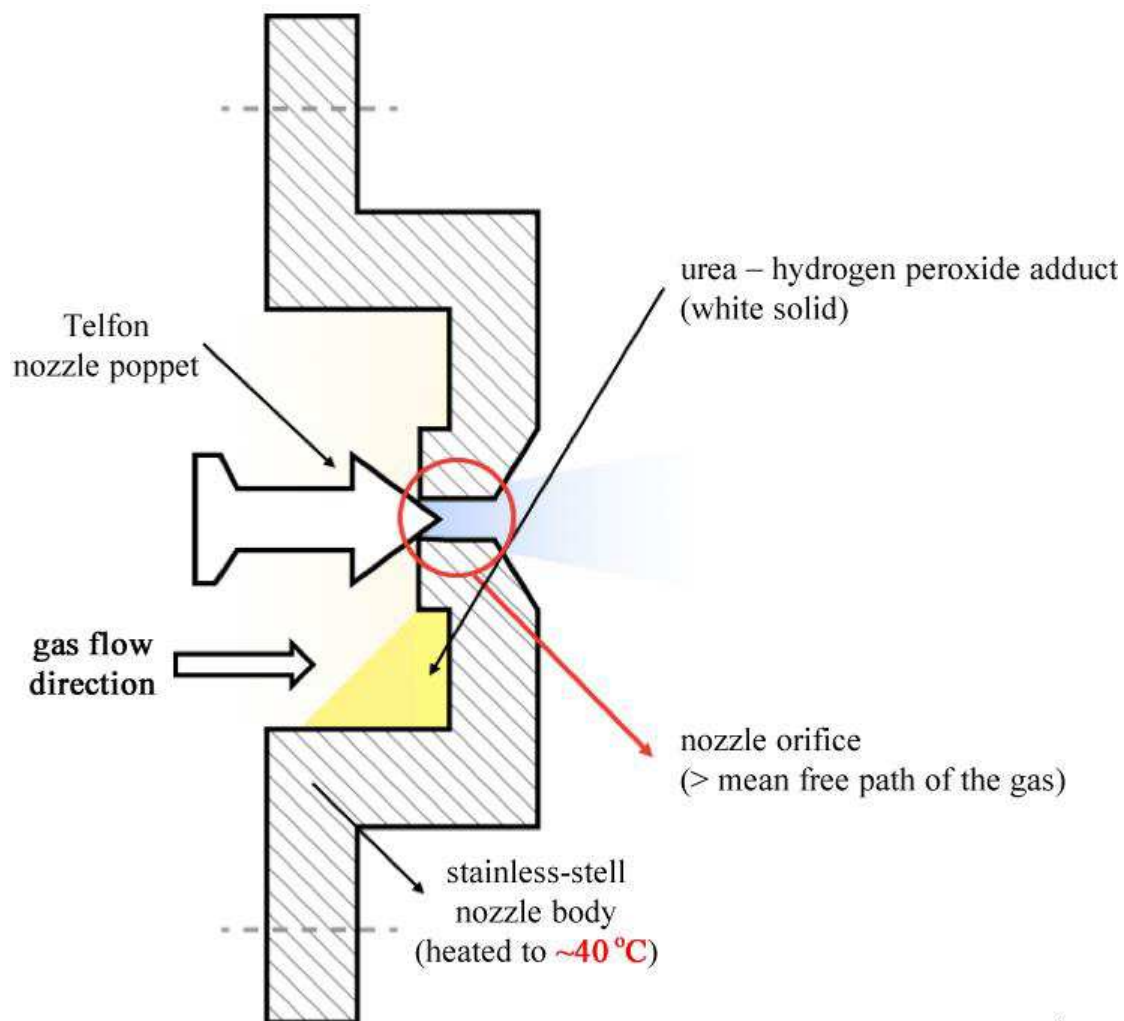


Figure 3.3.2 Cross-section of the stainless-steel nozzle cap.

A small amount of solid urea – hydrogen peroxide adduct was placed inside the nozzle cap, next to the nozzle orifice (highlighted as the yellow area in *Figure 3.3.2*), while heating wires were wrapped around the outside of the nozzle body. The amount of hydrogen peroxide released can be fine-tuned by changing the temperature. The released hydrogen peroxide gas then mixes with the formic acid containing sample gas before flowing through the nozzle orifice.

3.4 Transition Assignments

Previous studies of pure rotational spectra for various systems, including the hydrogen peroxide monomer [86], formic acid monomer [117], formic acid – water trimers [118], and water dimer [119], helped in identifying many observed transitions and optimizing experimental parameters. The intensity of the transition at 14829.109 MHz, originating from the hydrogen peroxide monomer, was used to monitor the hydrogen peroxide production while optimizing the nozzle temperature. Although the release of hydrogen peroxide can be accelerated by applying higher temperatures, its decomposition also is accelerated. Therefore, a mild heating temperature of $\sim 40^{\circ}\text{C}$ was chosen to compensate for the competition between the release and decomposition of hydrogen peroxide. The decomposition of hydrogen peroxide was monitored by observing a water dimer line at 12320.997 MHz.

Initially, multiple broadband rotational spectra in the 8–16 GHz range were recorded to search for the HP–FA–I or HP–FA–II conformers. However, just a few unknown lines were observed in the spectra, which might be attributed to the sensitivity limitations of the chirped-pulsed spectrometer. Exhaustive measurements were then performed using the cavity-based instrument. This time-consuming method was done by step-scanning over the whole operational window of the instrument automatically and then verifying each found transition manually. After several months of searching, more than 170 newly found lines were identified; it was obvious that not all of these could be resulting from the targeted complexes. Another challenge was the proximity of many lines, making transition assignments and spectrum fitting difficult; therefore, advanced analyses of the spectra were required.

3.4.1 The Closed-frequency Loop Method

In order to assign these observed transitions, the closed-frequency loop method was used. The concept of this method is straightforward and takes advantage of energy conservation. Starting from energy level $J(K_a, K_c) = 1(0, 1)$ in *Figure 3.4.1*, there are two different pathways, each involving two transitions, to reach the $J(K_a, K_c) = 2(1, 1)$ energy level (indicated in red). The sum of the frequencies in each pathway must be the same, within the measurement uncertainty. For the cavity-based FTMW spectrometer used in this thesis (see *Section 2.3.1*), the deviation should be within ± 2 kHz, i.e. the uncertainty level of measurement.

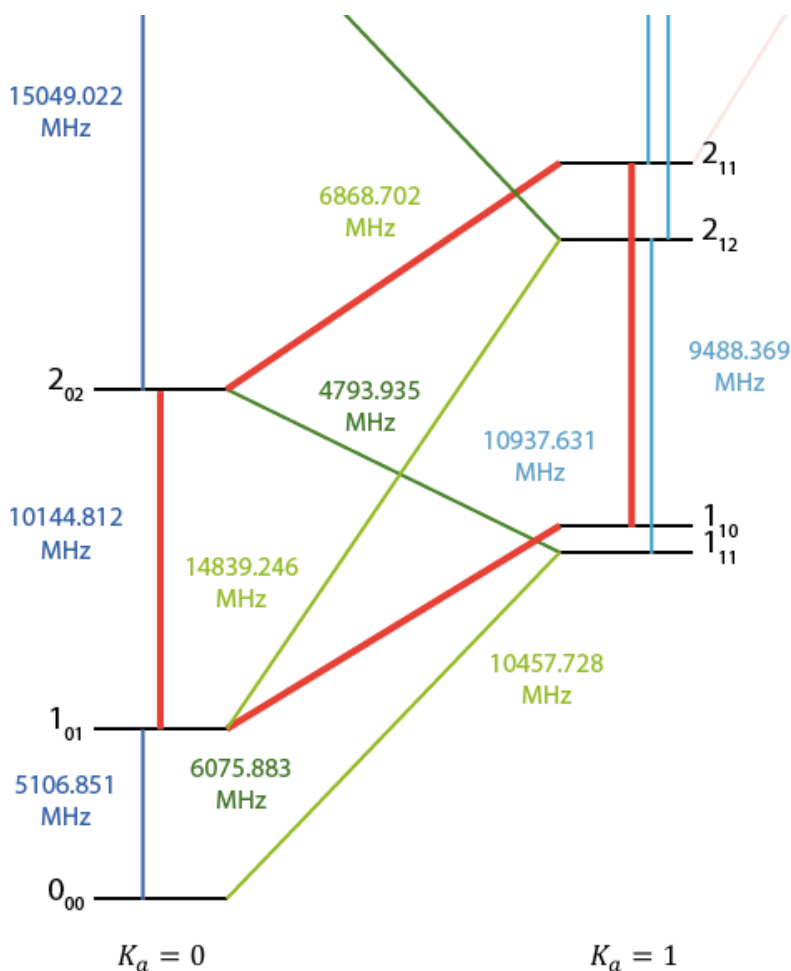


Figure 3.4.1 A closed-frequency loop (in red) in the rotational levels ($v = 0$) of HP-FA-I.

In general, a closed-frequency loop involves at least three transitions. A Python 3 script (see *Appendix B* or Ref. [120]) was coded to find possible loops by subtracting the frequency sums of candidate transitions in both pathways. If the difference was close to zero, within a predefined margin, a potential closed-frequency loop was identified. The script runs through all possible permutations of experimental frequencies. There is of course the possibility to find false positives, so it is important to compare the results with those predicted from the *ab initio* calculations. A firm assignment is likely if two or more connected closed-frequency loops can be found. Using this procedure, the quantum number assignments for two sets of transitions were acquired; both contain a-type and b-type transitions and are given in *Table 3.4.1*. In a preliminary fit, rotational constants and centrifugal distortion were obtained. By comparing the rotational constants with those from the *ab initio* calculations, it is evident that the HP-FA-I complex is the carrier of the transitions.

Table 3.4.1 Frequencies (in MHz) of the a-type and b-type transitions of HP-FA-I

$J'(K_a', K_c') \leftarrow J'(K_a'', K_c'')$	Transition type	$\nu=0$	$\nu=1$
1(0,1) \leftarrow 0(0,0)	a-type	5106.851	5107.584
1(1,1) \leftarrow 0(0,0)	b-type	10457.728	10457.831
1(1,0) \leftarrow 1(0,1)	b-type	6075.883	6075.166
2(0,2) \leftarrow 1(0,1)	a-type	10144.812	10147.023
2(1,1) \leftarrow 1(1,0)	a-type	10937.631	10939.417
2(1,2) \leftarrow 1(0,1)	b-type	14839.246	14839.902
2(0,2) \leftarrow 1(1,1)	b-type	4793.935	4796.776
2(1,2) \leftarrow 1(1,1)	a-type	9488.369	9489.655
2(1,1) \leftarrow 2(0,2)	b-type	6868.702	6867.560
3(0,3) \leftarrow 2(0,2)	a-type	15049.022	15044.800
3(1,2) \leftarrow 2(1,1)	a-type	16368.463	16363.714
3(0,3) \leftarrow 2(1,2)	b-type	10354.588	10351.921
3(1,3) \leftarrow 2(1,2)	a-type	-	14193.477
3(1,2) \leftarrow 3(0,3)	b-type	8188.143	8186.474

The measurement uncertainty is estimated to be ~ 2 kHz.

3.4.2 Intensity Analyses and Tunneling Splitting

As listed in *Table 3.4.1*, 27 transitions were assigned successfully by using the closed-frequency loop method. These transitions include a-type and b-type lines only, giving 14 four-frequency loops. Several observations could be made at this stage by analyzing the frequencies and line intensities. It is found that each transition is split into two components, which is indicative of a tunneling splitting. Furthermore, the intensity of transitions in one set of frequencies is always lower than that in the other. This indicates that the lower intensity transitions originate from energy levels with lower populations and thus from higher energy states. To distinguish these two sets of transitions, a vibrational quantum number ν was introduced. In addition, no c-type transitions could be measured in spite of a comparable dipole moment along the c-axis, as predicted by the *ab initio* calculations (see *Table 3.2.1*). Finally, the intensity ratio is close to 1:1 for the same rotational transition but different ν , implying that there are no effects from the spin statistics [121, 122]. An example is shown in *Figure 3.4.3*, where each transition is split by the Doppler effect due to the instrumental setup (see *Section 2.3.1*). As a result, this tunneling motion is clearly not the result of an interchange of two equivalent hydrogen atoms; otherwise, an intensity ratio of 1:3 would be observed due to the nature abundances of the *para*- and *ortho*- spin isomers of hydrogen.

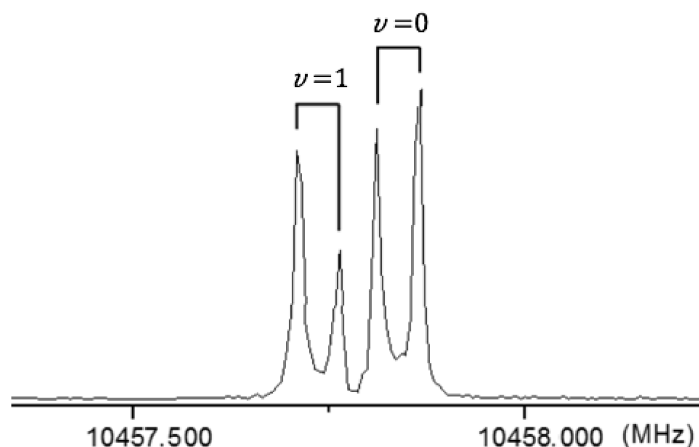


Figure 3.4.3 The $2(0, 2) \leftarrow 1(0, 1)$ transitions of HP-FA-I (averaged over 500 cycles).

A possible explanation for the observed splitting is a wagging-like tunneling motion of the non-hydrogen bonded H-atom from the hydrogen peroxide subunit, which tunnels from above or below the hydrogen-bonded ring parallel to the c-axis of HP-FA-I. Several approaches can be used to verify this proposal. One possibility is to measure transitions that are associated with the tunneling pathway; that is, if the proposed motion is correct, c-type transitions which connect the two tunneling states should be measurable. However, it would be nearly impossible to find the interstate c-type transitions without knowing the magnitude of the tunneling splitting. This splitting is related to the tunneling barrier and can be estimated using theoretical modeling, for example with the one-dimensional flexible model [123-125].

Because the scheme of the low J energy levels had been identified by using these intrastate a-type and b-type lines, the unknown was actually just the energy gap between two tunneling states, ΔE_{01} (see *Figure 3.4.4*). To estimate a value for ΔE_{01} , the system is assumed to have a Boltzmann distribution at a temperature of 2 K. Therefore, the relative intensities of the closed tunneling pairs with a frequency difference of less than 0.5 MHz, such as in the example in *Figure 3.4.3*, can be used in *Equation 2.1.10*. Since these lines were so close, both transitions could be observed simultaneously within one measurement in the cavity-based instrument. The evaluations lie in the range of 6 to 8 GHz, assuming an intensity ratio of 0.68 to 0.75. This information narrows down dramatically the search window for these interstate c-type transitions and these transitions were eventually found. The assignments were confirmed with the closed-frequency loop method. Altogether seven interstate c-type transitions were measured (see *Table 3.4.2*), and ΔE_{01} was determined to be 7668.549 GHz experimentally. This is consistent with the estimated value assuming a Boltzmann distribution.

A stick spectrum presented in *Figure 3.4.5* demonstrates the density of lines in the 12 to 15 GHz region and the complexity of the spectroscopic assignment process. All transitions found in

this region are plotted in the spectrum. The lines are colour-labelled according to the molecular carrier. For clarity, lines corresponding to different molecules or complexes are also plotted with different lengths. Note the significant number of still unassigned transitions, which may belong to a number of species, such as, for example, hydrogen peroxide dimer, larger (formic acid)_n – (H₂O)_m clusters, or dioxygen containing complexes.

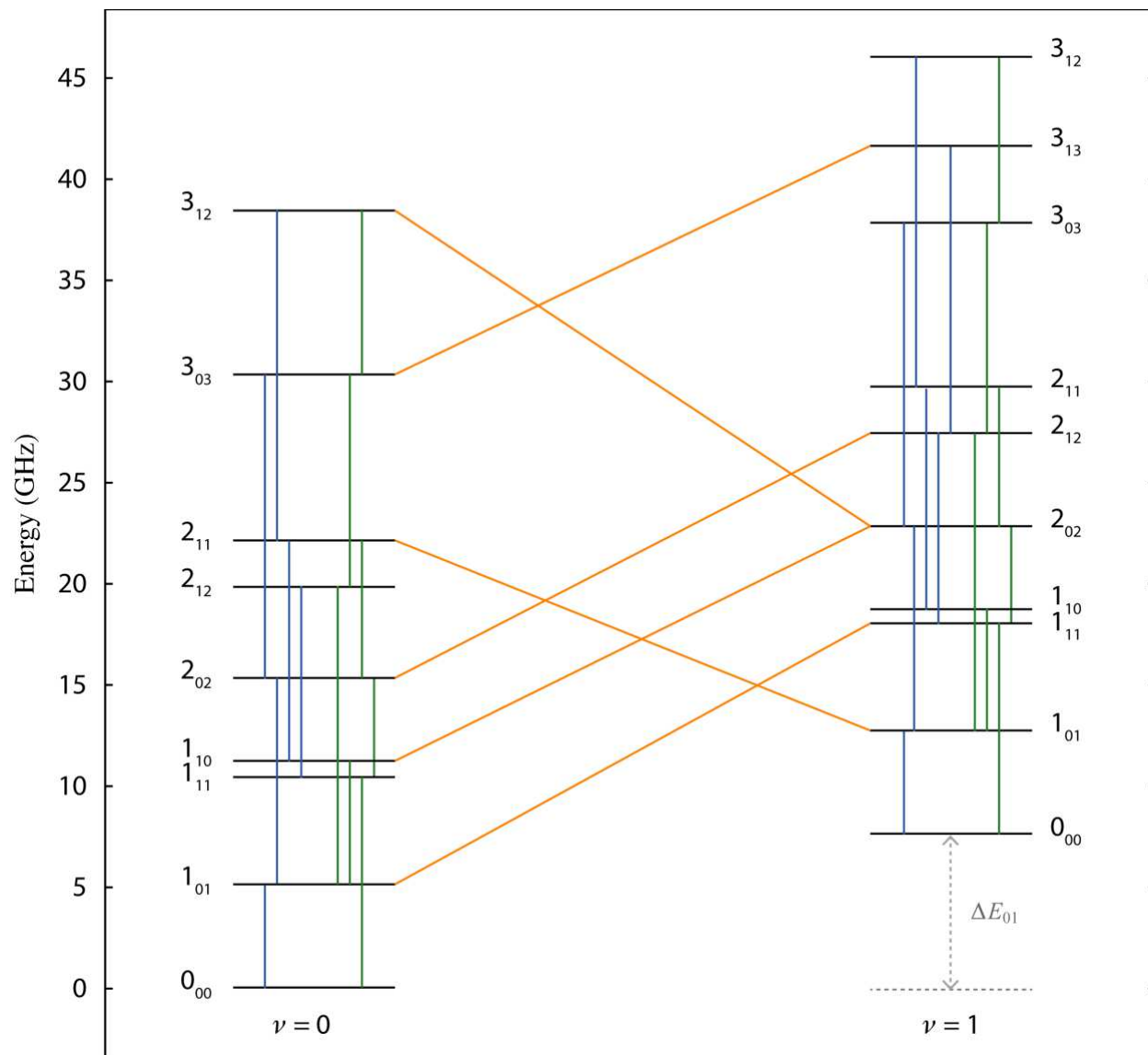


Figure 3.4.4 The energy-level diagram with all measured transitions of HP-FA-I.

All measured transitions are indicated in this diagram. Blue, green, and orange colours represent a-type, b-type, and c-type transitions, respectively.

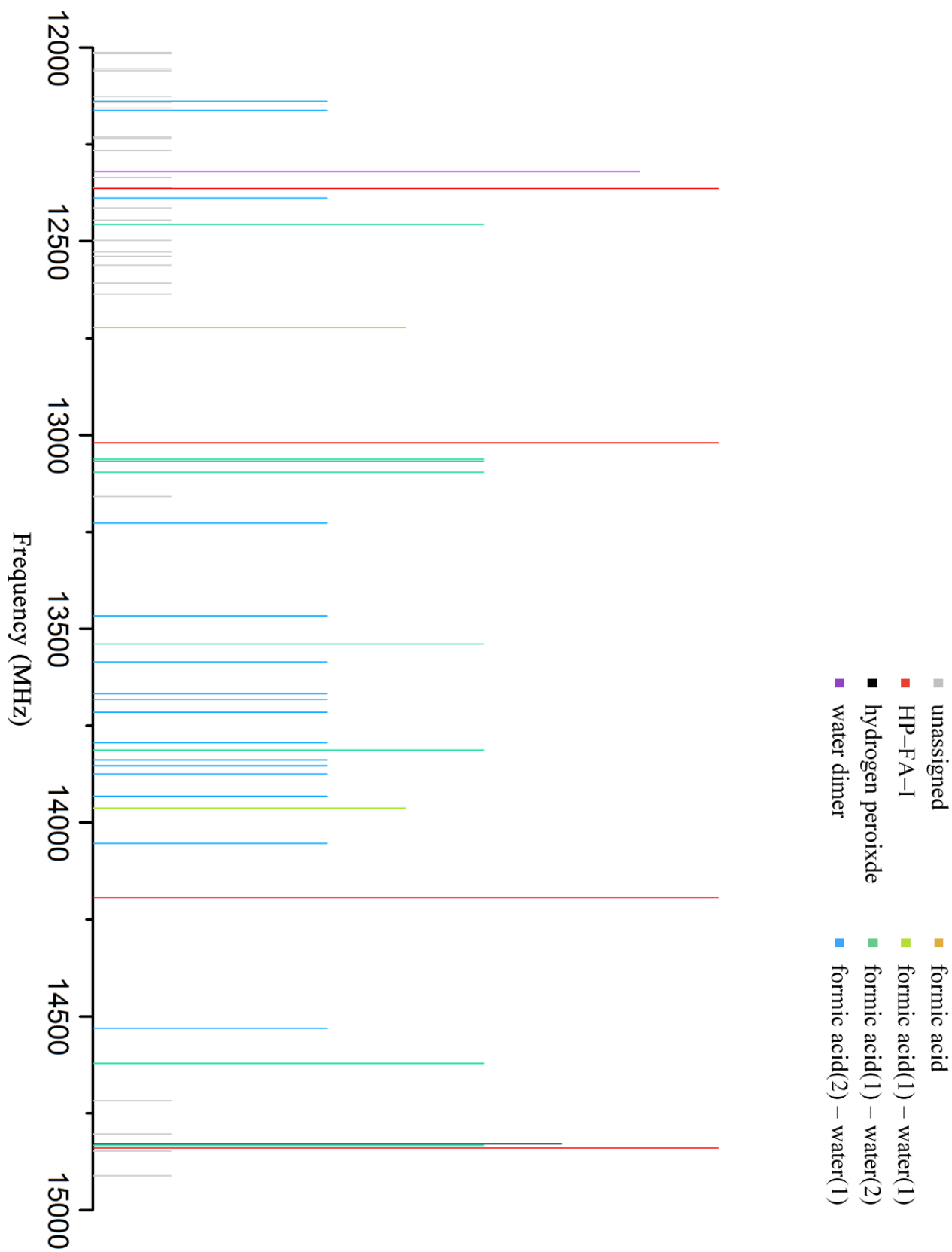


Figure 3.4.5 A stick spectrum of all lines recorded between 12 and 15 GHz.

Table 3.4.2 Frequencies (in MHz) of the observed interstate c-type transitions of HP-FA-I

$J'(K_a', K_c') \leftarrow J'(K_a'', K_c'')$	$\nu = 1 \leftarrow \nu = 0$	$\nu = 0 \leftarrow \nu = 1$
1(1,1) \leftarrow 1(0,1)	13019.529	-
2(1,1) \leftarrow 1(0,1)	-	9344.232
2(0,2) \leftarrow 1(1,0)	11740.422	-
2(1,2) \leftarrow 2(0,2)	12364.372	-
3(1,2) \leftarrow 2(0,2)	-	15565.672
3(0,3) \leftarrow 2(1,1)	15847.591	-
3(1,3) \leftarrow 3(0,3)	11508.827	-

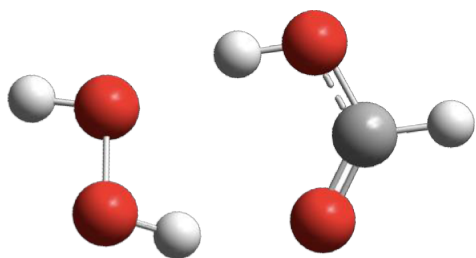
The measurement uncertainty is estimated to be ~ 2 kHz.

3.5 Intrinsic Reaction Coordinate Calculations

To verify the proposed tunneling motion theoretically, intrinsic reaction coordinate (IRC) calculations were carried out at the MP2/6-311++g(2d,p) level of theory (see *Section 2.5 (a)*). One of the key steps in these calculations is to predict the structure of the transition state from the assumed tunneling path. If the structure is correct, it shall possess exactly one imaginary frequency which corresponds to the vibrational motion along the tunneling coordinate. Once the optimized structure of the transition state, denoted by HP-FA-I*, is obtained, it is used as the input for an IRC calculation. If the calculation has terminated normally, and the transition state has relaxed to the minimum, one then can say that the proposed tunneling motion is theoretically reasonable.

Initially, the structure of the transition state was guessed to be planar. However, the transition state found is actually non-planar, as shown in *Figure 3.5.1*. As a result, the calculated IRC path is an asymmetric profile, as seen in *Figure 3.5.2*, and another equivalent transition state could be obtained by flipping its parity. This can be visualized by looking at the non-hydrogen-bonded H-atom in the hydrogen peroxide subunit and recognizing that a motion of this H-atom to above the molecular ring of the complex is different from its motion to below that ring. This transition state indicates a $6.9 \text{ kJ}\cdot\text{mol}^{-1}$ barrier and was concluded to be theoretically reasonable.

(a) HP-FA-I*: top view



(b) HP-FA-I*: side view

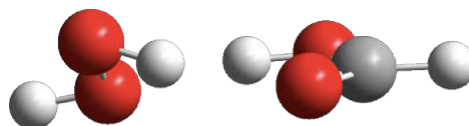


Figure 3.5.1 Transition state found and used in verifying the proposed tunneling motion.

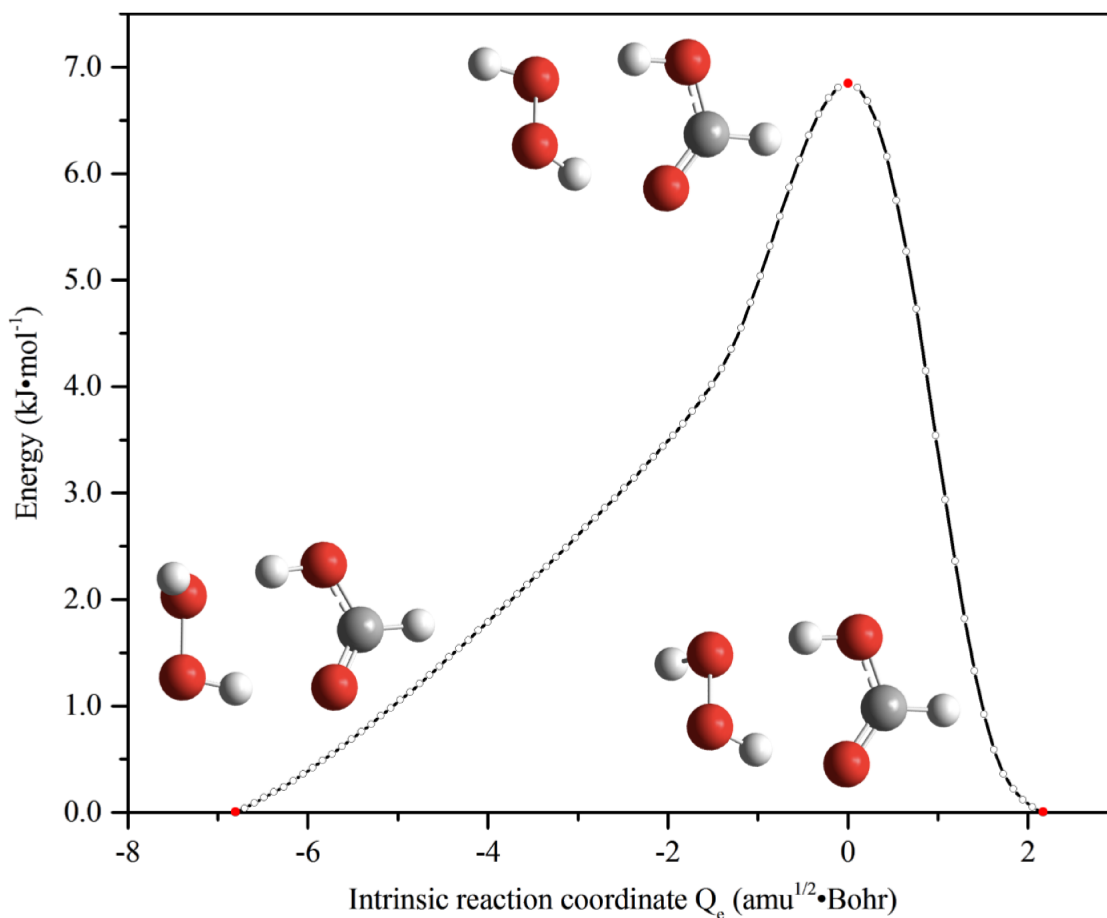


Figure 3.5.2 The intrinsic reaction coordinate for the tunneling motion in HP-FA-I.

The barrier to the tunneling motion is calculated to be $6.9 \text{ kJ}\cdot\text{mol}^{-1}$. Structures near a red dot represent the geometry at that point.

3.6 Fitting of The Spectroscopic Constants

After several failed trials in fitting the spectroscopic constants of HP–FA–I, it was concluded that the two tunneling states could not be fitted separately even by introducing additional higher-order centrifugal distortion terms. Similar observations have been made before in the cases of the isopropanol – water dimer [123] and the benzoic acid – formic acid dimer [126], for example. In those instances, it was found that interactions between the two tunneling states cause slight shifts of rotational energy levels. The mechanism behind this interaction is rotation-vibration or named Coriolis coupling [127]. For the case of HP–FA–I, the measured interstate, c-type transitions made it possible to fit all measured transitions simultaneously and determine the Coriolis coupling parameters.

In order to fit the spectrum, the following Hamiltonian was considered [123]:

$$\hat{H} = H_0^R + H_1^R + H^{CD} + H^{CC}$$

(Equation 3.6.1),

where, H_0^R and H_1^R are the rigid-body rotational Hamiltonians for the $\nu = 0$ and $\nu = 1$ states, respectively. H^{CD} is the centrifugal distortion Hamiltonian that is assumed to be the same for both states and H^{CC} describes the Coriolis coupling between the two tunneling states. Since the first three terms in the equation have been described previously (See *Section 2.1*), the focus here is on the H^{CC} term, which cannot be solved directly. By expanding H^{CC} to the second order in the angular momentum, here obtains:

$$H^{CC} = \Delta E_{01} + F_a \times (P_b P_c + P_c P_b) + F_b \times (P_a P_c + P_c P_a)$$

(Equation 3.6.2),

where ΔE_{01} is the magnitude of the tunneling splitting; F_a , F_b are the Coriolis coupling parameters; P_g ($g = a, b, \text{ or } c$) represents the angular momentum operator for the g -axis. Because the tunneling

motion is occurring along the c-axis, the $F_c \times (P_a P_b + P_b P_a)$ term was not included in Equation 3.6.2 [128]. Since the calculated structure of HP-FA-I is a near prolate-top species, the Watson's S-reduction Hamiltonian in its Ir representation [129] was used in the fitting process.

Finally, based on the assigned transitions given in Table 3.4.1 and Table 3.4.2 and the choice of an appropriate \hat{H} for the system, spectroscopic constants of HP-FA-I were successfully fitted. The resulting parameters are listed in Table 3.6.1; σ is the standard deviation of the fit and N is the numbers of fitted transitions. The standard deviation of the fit σ , is 0.502 kHz, which is of the same order of magnitude as the measurement uncertainty. The relatively small values of the centrifugal distortion constants (in the kHz range) in Table 3.6.1 indicate the rigidity of the complex. The small difference in rotational constants between two tunneling states indicates a high barrier of tunneling motion, which is consistent with both experimental and theoretical results.

Table 3.6.1 The fitted spectroscopic constants of HP-FA-I

ν	0	1
A /MHz	8266.910(3)	8266.594(5)
B /MHz	2916.030(9)	2916.160(6)
C /MHz	2190.848(8)	2191.258(2)
D_J /kHz		2.002(1)
D_{JK} /kHz		10.350(6)
d_J /kHz		0.460(1)
ΔE_{01} /MHz		7668.551(1)
F_a /MHz		16.530(4)
F_b /MHz		5.380(1)
σ /kHz		0.502
N		34

The numbers in parentheses are the uncertainties in units of the least significant digits.

3.7 Analyses of the Electron Density Topology

From the small differences between experimental and calculated the rotational constants, this suggests that the *ab initio* structure is quite accurate. One can therefore use the optimized geometry to acquire a deeper understanding of the intermolecular interactions in HP-FA-I. Analyses of the electron density topology of the system can provide deeper insights into the roles of hydrogen peroxide and formic acid within the system, in particular in terms of hydrogen bonding interactions.

The concept of electron density topology analysis was first introduced by Richard F. W. Bader in his quantum theory of atoms in molecules (QTAIM or AIM) [55, 56]. His work has then been extended to the non-covalent interactions (NCI) method [57] and the electron localization function [130]. In the QTAIM approach, a gradient vector map of the electron density, ρ , is produced, in which trajectories trace the path of steepest ascent of the electron density. Sets of these trajectories terminate at the nuclei (attractors), which represent maxima of the electron density. The region of space that is filled by trajectories terminating at a specific nucleus is called the atomic basin belonging to that nucleus. Properties of a specific atom, such as electron population or atomic volume, can be extracted by integrating over the volume of the atomic basin.

Another important concept in the QTAIM approach are critical points, which are defined by having a vanishing gradient in ρ (except at infinity). They are further classified by considering the second derivative of ρ at that point, specifically, the diagonal elements of the second derivative tensor of ρ , the so-called Hessian. If all three diagonal elements are negative, the critical point is a local maximum in ρ and corresponds to a nucleus. If two elements are negative, and one positive, the critical point is a bond critical point (BCP). A BCP is connected to two nuclei by trajectories in the gradient vector map, which are called a bond path. A ring critical point has one negative and two positive diagonal elements in the Hessian, and a cage critical point has three positive diagonal

elements [56]. *Figure 3.7.1* shows a QTAIM plot of the HP-FA-I complex. Of particular interest here are the BCPs and bond paths, which correspond to the hydrogen bonding interactions. The hydrogen bonds lead to the formation of a seven-membered ring, which is identified in the QTAIM plot by a ring critical point.

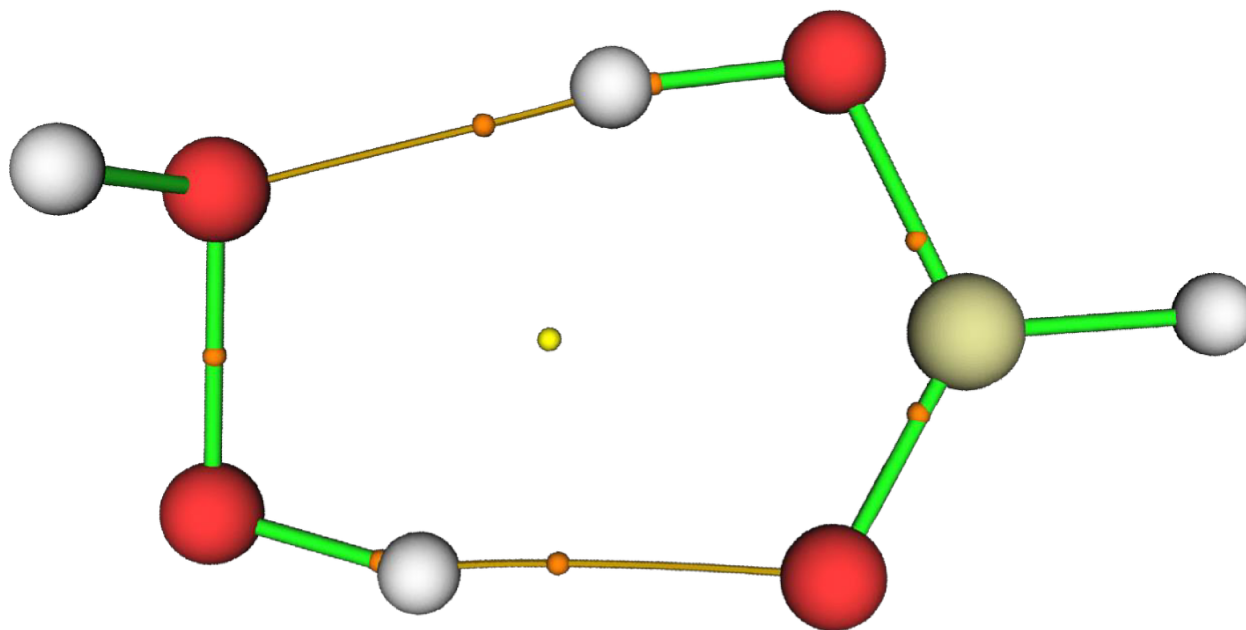


Figure 3.7.1 **The critical points and the bond paths of HP-FA-I found in the QTAIM analysis.** The small orange and yellow balls indicate the bond critical points and a ring critical point in HP-FA-I, respectively. The thin orange bars represent the bond paths of the hydrogen bonds in the system.

3.7.1 Visualization of Non-Covalent Interactions

Non-covalent interaction (NCI) analysis is an electron density topology analysis that can be used to visualize weak interactions in a molecule or complex that cannot be effectively represented by the traditional ball-and-stick model [57]. With an NCI analysis and the resultant plot, one can identify types of interactions and their position in real space and their relative strengths.

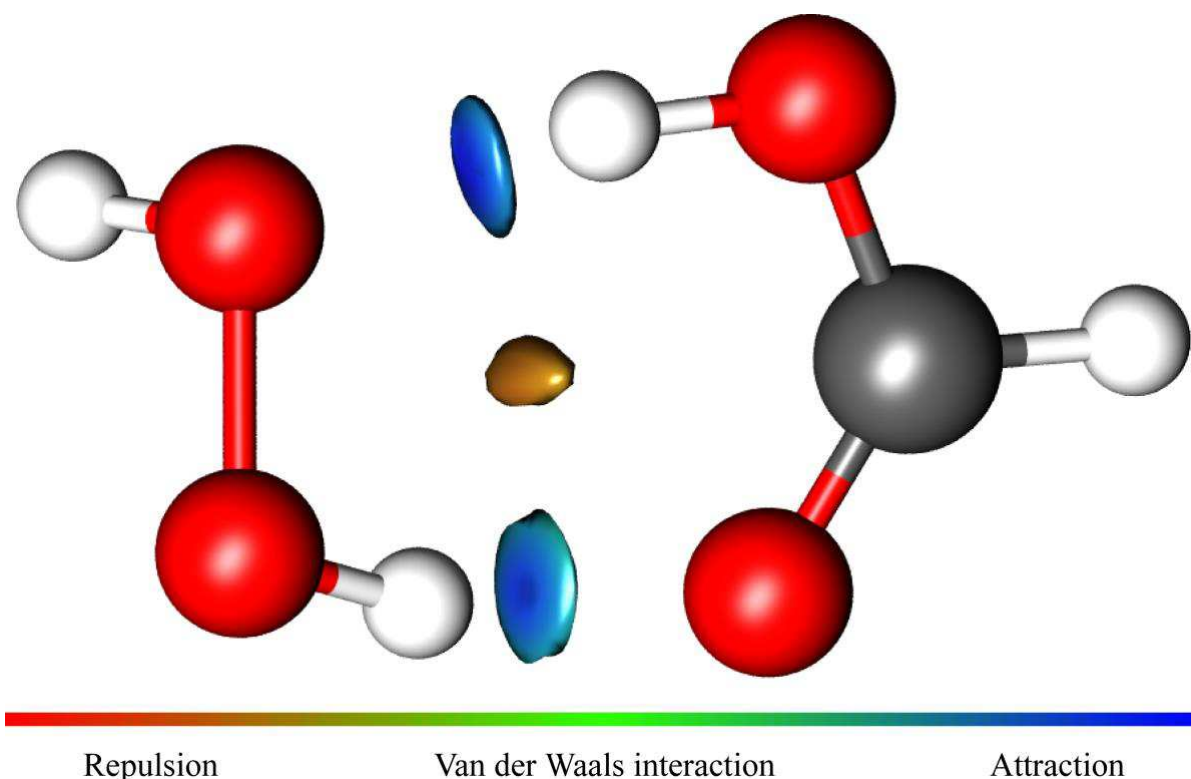


Figure 3.7.2 The weak interactions in HP-FA-I unveiled by an NCI analysis.

An NCI plot for HP-FA-I is shown in *Figure 3.7.2*. In the figure, isosurfaces of a reduced electron density gradient s of 0.5 a.u. are coloured in accordance with the value of $\text{sign}(\lambda_2)\rho$, where ρ is the electron density and λ_2 is the second eigenvalue of the Hessian matrix of ρ . Two blue disks indicate the hydrogen bonds, represented by HO...HO (upper) and OH...O=C (lower), while a brown bean suggests a repulsion from the ring strain. It can be seen that HO...HO disk is slightly darker, which implies a stronger interaction than OH...O=C.

3.7.2 Hydrogen Bonding Evaluations

The NCI plot indicates that although the ring strain is a system destabilizing factor, the two hydrogen bonds are so strong that they can glue two molecules together to form a binary complex. This phenomenon raises the question of how strong the binding is. To give a quantitative description, properties of the BCPs of the hydrogen bonds are examined, and the results are presented in *Table 3.7.1*, where the following notations are used: the hydrogen bond length $r(\text{O}\cdots\text{H})$, electron density ρ , Laplacian of electron density $\nabla^2\rho$, electronic potential energy density $V(r)$, and hydrogen bonding energy E_{HB} , which can be estimated either by $V(r)$ or ρ .

Table 3.7.1 BCP properties and energy evaluation for H-bonds in HP-FA-I and HP-FA-I*

	HP-FA-I		HP-FA-I*	
	HO \cdots HO	OH \cdots O=C	HO \cdots HO	OH \cdots O=C
$r(\text{O}\cdots\text{H}) / \text{\AA}$	1.772	1.820	1.814	1.861
$\rho / \text{a.u.}$	0.03681	0.03299	0.02979	0.02982
$\nabla^2\rho / \text{a.u.}$	0.11839	0.11129	0.11610	0.10452
$V(r) / \text{a.u.}$	-0.03287	-0.02790	-0.02582	-0.02447
$E_{\text{HB}}[V(r)] / \text{kJ}\cdot\text{mol}^{-1}$	43.2	36.6	33.9	32.1
$E_{\text{HB}}(\rho) / \text{kJ}\cdot\text{mol}^{-1}$	41.4	37.1	33.5	33.6

Based on work by Espinosa *et al.* [131], the relationship between $V(r)$ and E_{HB} at the corresponding BCP is approximated as:

$$E_{\text{HB}}[V(r)] = \frac{1}{2} V(r)$$

(Equation 3.7.1).

On the other hand, a simple linear regression between E_{HB} and ρ using empirical regression coefficients provides another way to estimate the energy for hydrogen bonding [132, 133]:

$$E_{\text{HB}}(\rho) = A\rho + B$$

(Equation 3.7.2),

where $A = 268 \text{ kcal}\cdot\text{mol}^{-1}\cdot(\text{a.u.})^{-1}$ and $B = 0$ are obtained from 94 different H-bonded complexes [133]. Both methods provide similar estimates for the energy of the hydrogen bonds. Based on the energies and lengths of hydrogen bonds in HP–FA–I, it is obvious that hydrogen peroxide is slightly more of a hydrogen bond acceptor than a donor.

3.8 Summary

The pure rotational spectrum of the most stable isomer of the hydrogen peroxide – formic acid complex, HP–FA–I, was measured using a cavity-based FTMW spectrometer. This is the first high-resolution study of a complex containing hydrogen peroxide in the gas phase. By using the closed-frequency loop method and intensity analyses, 34 rotational transitions were assigned and used to fit the spectroscopic constants of HP–FA–I. In addition to the Doppler doublet, a tunneling splitting was observed. The magnitude of the splitting was determined from the frequencies of seven interstate c-type transitions. A tunneling motion is proposed to explain the reason for the splitting, which is a wagging-like motion that allows the free O–H group to tunnel from one side of the hydrogen bonded ring to the other, parallel to the c-axis of HP–FA–I. This tunneling motion was also verified to be a theoretically reasonable path using IRC calculations, where a tunneling barrier of $6.9 \text{ kJ}\cdot\text{mol}^{-1}$ was found. Additional insights into the intermolecular interactions within the HP–FA–I complex were gained with QTAIM and NCI analyses. Finally, by using QTAIM, the properties of BCP at the hydrogen bonds were determined so that the energy of hydrogen bonding could be evaluated. The results show that hydrogen peroxide slightly favors being a proton acceptor than a donor in HP–FA–I.

CHAPTER 4

Concluding Remarks

The first gas-phase study of a complex that involves a hydrogen peroxide subunit was accomplished by using rotational spectroscopy. The results show that hydrogen peroxide can form a stable van der Waals complex with formic acid through hydrogen bonding. Both hydrogen peroxide and formic acid occur in nature and are of atmospheric relevance. These molecules are involved in processes, such as formation of acid rain and the aggregation of molecules to produce fine particulate matters [134]. Intermolecular interactions play a role in those processes, and the present study provides some detailed insights as a foundation for further studies of hydrogen peroxide containing complexes.

In conclusion, this work demonstrates that the complexity of the hydrogen peroxide spectrum that results from the torsional tunnelling motions of hydrogen peroxide can be reduced by introducing formic acid, which can ‘hold’ one of the two hydroxyl groups of hydrogen peroxide tightly. The pure rotational spectra of the hydrogen peroxide – formic acid complex, recorded with a cavity-based FTMW spectrometer, reveal splitting of rotational transitions into two components. This splitting is attributed to a tunneling motion of the free hydroxyl group of hydrogen peroxide tunnels from above or below the ring to the other side, parallel to the c-axis of the complex. The tunneling path was also studied using *ab initio* calculations at the MP2/6-311++g(2d,p) level of theory. Compared with a previous study on the formic acid – water system [118], analyses of the electron density topology suggest that formic acid has much stronger intermolecular interactions with hydrogen peroxide than with water; this is consistent with previous *ab initio* studies [113,114].

BIBLIOGRAPHY

- [1] Rosenfeld, D. and Lensky, I.M., 1998. Satellite-based insights into precipitation formation processes in continental and maritime convective clouds. *Bulletin of the American Meteorological Society*, **79**, pp.2457-2476.
- [2] Blaney, B.L. and Ewing, G.E., 1976. Van der Waals molecules. *Annual Review of Physical Chemistry*, **27**, pp.553-584.
- [3] Grimme, S., 2004. Accurate description of van der Waals complexes by density functional theory including empirical corrections. *Journal of Computational Chemistry*, **25**, pp.1463-1473.
- [4] Chang, H.C., Jiang, J.C., Chen, T.Y., Wang, H.S., Li, L.Y., Hung, W.W. and Lin, S.H., 2013. Specific interactions between the quaternary ammonium oligoether-based ionic liquid and water as a function of pressure. *Physical Chemistry Chemical Physics*, **15**, pp.12734-12741.
- [5] Tso, T.L. and Lee, E.K., 1985. Role of hydrogen bonding studied by the FTIR spectroscopy of the matrix-isolated molecular complexes, dimer of water, water. carbon dioxide, water. carbon monoxide and hydrogen peroxide. n carbon monoxide in solid molecular oxygen at 12-17 K. *The Journal of Physical Chemistry*, **89**, pp.1612-1618.
- [6] Surewicz, W.K., Mantsch, H.H. and Chapman, D., 1993. Determination of protein secondary structure by Fourier transform infrared spectroscopy: a critical assessment. *Biochemistry*, **32**, pp.389-394.
- [7] Bondybey, V.E. and English, J.H., 1981. Laser induced fluorescence of metal clusters produced by laser vaporization: Gas phase spectrum of Pb₂. *The Journal of Chemical Physics*, **74**, pp.6978-6979.

- [8] Nakajima, A., Hirano, M., Hasumi, R., Kaya, K., Watanabe, H., Carter, C.C., Williamson, J.M. and Miller, T.A., 1997. High-Resolution Laser-Induced Fluorescence Spectra of 7-Azaindole–Water Complexes and 7-Azaindole Dimer. *The Journal of Physical Chemistry A*, **101**, pp.392-398.
- [9] Gibson, E.M., Jones, A.C., Taylor, A.G., Bouwman, W.G., Phillips, D. and Sandell, J., 1988. Laser-induced fluorescence spectroscopy of 4-aminobenzonitrile, 4-(N, N-dimethylamino) benzonitrile, and their van der Waals complexes in a supersonic jet. *The Journal of Physical Chemistry*, **92**, pp.5449-5455.
- [10] Tolstoy, P.M., Smirnov, S.N., Shenderovich, I.G., Golubev, N.S., Denisov, G.S. and Limbach, H.H., 2004. NMR studies of solid state—solvent and H/D isotope effects on hydrogen bond geometries of 1:1 complexes of collidine with carboxylic acids. *Journal of Molecular Structure*, **700**, pp.19-27.
- [11] Schnell, I., Brown, S.P., Low, H.Y., Ishida, H. and Spiess, H.W., 1998. An investigation of hydrogen bonding in benzoxazine dimers by fast magic-angle spinning and double-quantum ¹H NMR spectroscopy. *Journal of the American Chemical Society*, **120**, pp.11784-11795.
- [12] Arnold, W.D. and Oldfield, E., 2000. The chemical nature of hydrogen bonding in proteins via NMR: J-couplings, chemical shifts, and AIM theory. *Journal of the American Chemical Society*, **122**, pp.12835-12841.
- [13] Townes, C.H. and Schawlow, A.L., 2013. *Microwave spectroscopy*. Courier Corporation.
- [14] Bernath, P.F., 2015. *Spectra of atoms and molecules*. Oxford University Press.
- [15] Levine, I.N., Busch, D.H. and Shull, H., 2009. *Quantum chemistry (Vol. 6)*. Upper Saddle River, NJ: Pearson Prentice Hall.

- [16] Varshalovich, D.A., Moskalev, A.N. and Khersonskii, V.K.M., 1988. *Quantum Theory of Angular Momentum*.
- [17] Courtney, M., Spellmeyer, N., Jiao, H. and Kleppner, D., 1995. Classical, semiclassical, and quantum dynamics in the lithium Stark system. *Physical Review A*, **51**, p.3604.
- [18] Atkins, P., De Paula, J. and Keeler, J., 2018. *Atkins' physical chemistry*. Oxford university press.
- [19] Wu, Y. and Yang, X., 2007. Strong-coupling theory of periodically driven two-level systems. *Physical Review Letters*, **98**, p.013601.
- [20] Mukamel, S., 1999. *Principles of nonlinear optical spectroscopy (No. 6)*. Oxford University Press on Demand.
- [21] Blum, K., 2012. *Density matrix theory and applications (Vol. 64)*. Springer Science & Business Media.
- [22] Von Neumann, J., 1927. Wahrscheinlichkeitstheoretischer aufbau der quantenmechanik. *Nachrichten von der Gesellschaft der Wissenschaften zu Göttingen, Mathematisch-Physikalische Klasse*, **1927**, pp.245-272.
- [23] Allen, L. and Eberly, J.H., 2012. *Optical resonance and two-level atoms*. Courier Corporation.
- [24] Arecchi, F. and Bonifacio, R., 1965. Theory of optical maser amplifiers. *IEEE Journal of Quantum Electronics*, **1**, pp.169-178.
- [25] Kantrowitz, A. and Grey, J., 1951. A high intensity source for the molecular beam. Part I. Theoretical. *Review of Scientific Instruments*, **22**, pp.328-332.

- [26] McAfee Jr, K.B., Hughes, R.H. and Wilson Jr, E.B., 1949. A Stark-Effect Microwave Spectrograph of High Sensitivity. *Review of Scientific Instruments*, **20**, pp.821-826.
- [27] Hughes, R.H. and Wilson Jr, E.B., 1947. A microwave spectrograph. *Physical Review*, **71**, p.562.
- [28] Hernández, G., 1988. *Fabry–Pérot interferometers (No. 3)*. Cambridge University Press.
- [29] Balle, T.J. and Flygare, W.H., 1981. Fabry–Pérot cavity pulsed Fourier transform microwave spectrometer with a pulsed nozzle particle source. *Review of Scientific Instruments*, **52**, pp.33-45.
- [30] Campbell, E.J., Buxton, L.W., Balle, T.J. and Flygare, W.H., 1981. The theory of pulsed Fourier transform microwave spectroscopy carried out in a Fabry–Pérot cavity: Static gas. *The Journal of Chemical Physics*, **74**, pp.813-828.
- [31] Campbell, E.J., Buxton, L.W., Balle, T.J., Keenan, M.R. and Flygare, W.H., 1981. The gas dynamics of a pulsed supersonic nozzle molecular source as observed with a Fabry–Pérot cavity microwave spectrometer. *The Journal of Chemical Physics*, **74**, pp.829-840.
- [32] Brown, G.G., Dian, B.C., Douglass, K.O., Geyer, S.M., Shipman, S.T. and Pate, B.H., 2008. A broadband Fourier transform microwave spectrometer based on chirped pulse excitation. *Review of Scientific Instruments*, **79**, p.053103.
- [33] Chou, J., Han, Y. and Jalali, B., 2003. Adaptive RF-photonics arbitrary waveform generator. *IEEE Photonics Technology Letters*, **15**, pp.581-583.
- [34] Chuang, C., Hawley, C.J., Emilsson, T. and Gutowsky, H.S., 1990. Computer-based controller and averager for the Balle-Flygare spectrometer. *Review of Scientific Instruments*, **61**, pp.1629-1635.

- [35] Grabow, J.U., 2011. Fourier transform microwave spectroscopy measurement and instrumentation. *Handbook of High-Resolution Spectroscopy*.
- [36] Xu, Y. and Jäger, W., 1997. Evidence for heavy atom large amplitude motions in RG-cyclopropane van der Waals complexes (RG= Ne, Ar, Kr) from rotation-tunneling spectroscopy. *The Journal of Chemical Physics*, **106**, pp.7968-7980.
- [37] Schnell, M., Banser, D. and Grabow, J.U., 2004. Coaxially aligned electrodes for Stark-effect applied in resonators using a supersonic jet Fourier transform microwave spectrometer. *Review of Scientific Instruments*, **75**, pp.2111-2115.
- [38] Grabow, J.U. and Stahl, W., 1990. A pulsed molecular beam microwave Fourier transform spectrometer with parallel molecular beam and resonator axes. *Zeitschrift für Naturforschung A*, **45**, pp.1043-1044.
- [39] Andresen, U., Dreizler, H., Grabow, J.U. and Stahl, W., 1990. An automatic molecular beam microwave Fourier transform spectrometer. *Review of Scientific Instruments*, **61**, pp.3694-3699.
- [40] Dreizler, H., 1986. Experiences with microwave Fourier transform spectroscopy of molecular gases. *Molecular Physics*, **59**, pp.1-28.
- [41] Dempster, S.P., Sukhorukov, O., Lei, Q.Y. and Jäger, W., 2012. Rotational spectroscopic study of hydrogen cyanide embedded in small ^4He clusters. *The Journal of Chemical Physics*, **137**, p.174303.
- [42] McGurk, J.C., Schmalz, T.G. and Flygare, W.H., 1974. Fast passage in rotational spectroscopy: Theory and experiment. *The Journal of Chemical Physics*, **60**, pp.4181-4188.

- [43] Parr, R.G., Craig, D.P. and Ross, I.G., 1950. Molecular orbital calculations of the lower excited electronic levels of benzene, configuration interaction included. *The Journal of Chemical Physics*, **18**, pp.1561-1563.
- [44] Slater, J.C., 1951. A simplification of the Hartree-Fock method. *Physical Review*, **81**, p.385.
- [45] Møller, C. and Plesset, M.S., 1934. Note on an approximation treatment for many-electron systems. *Physical Review*, **46**, p.618.
- [46] Fano, U., 1961. Effects of configuration interaction on intensities and phase shifts. *Physical Review*, **124**, p.1866.
- [47] Feng, G., Gou, Q., Evangelisti, L. and Caminati, W., 2014. Frontiers in Rotational Spectroscopy: Shapes and Tunneling Dynamics of the Four Conformers of the Acrylic Acid—Difluoroacetic Acid Adduct. *Angewandte Chemie International Edition*, **53**, pp.530-534.
- [48] Thomas, J., Liu, X., Jäger, W. and Xu, Y., 2015. Unusual H-Bond Topology and Bifurcated H-bonds in the 2-Fluoroethanol Trimer. *Angewandte Chemie International Edition*, **54**, pp.11711-11715.
- [49] Krishnan, R.B.J.S., Binkley, J.S., Seeger, R. and Pople, J.A., 1980. Self-consistent molecular orbital methods. XX. A basis set for correlated wave functions. *The Journal of Chemical Physics*, **72**, pp.650-654.
- [50] Parr, R.G., 1980. Density functional theory of atoms and molecules. In *Horizons of Quantum Chemistry* (pp. 5-15). Springer, Dordrecht.
- [51] Becke, A.D., 1993. Becke's three parameter hybrid method using the LYP correlation functional. *The Journal of Chemical Physics*, **98**, pp.5648-5652.

- [52] Frisch, M., Trucks, G., Schlegel, H., Scuseria, G., Robb, M., Cheeseman, J., Zakrzewski, V., Montgomery Jr, J., Stratmann, R., Burant, J. and Dapprich, S., Gaussian 09, Gaussian, Inc., Pittsburgh, PA, 2009;(b) Dalton 2.0 Program Package.
- [53] Western, C.M., 2017. PGOPHER: A program for simulating rotational, vibrational and electronic spectra. *Journal of Quantitative Spectroscopy and Radiative Transfer*, **186**, pp.221-242.
- [54] Pickett, H.M., 2009. SPFIT/SPCAT package.
- [55] Bader, R.F., 1991. A quantum theory of molecular structure and its applications. *Chemical Reviews*, **91**, pp.893-928.
- [56] Bader, R.F., 1990. *Atoms in molecules*. John Wiley & Sons, Ltd.
- [57] Johnson, E.R., Keinan, S., Mori-Sanchez, P., Contreras-Garcia, J., Cohen, A.J. and Yang, W., 2010. Revealing noncovalent interactions. *Journal of the American Chemical Society*, **132**, pp.6498-6506.
- [58] Lu, T. and Chen, F., 2012. Multiwfn: a multifunctional wavefunction analyzer. *Journal of Computational Chemistry*, **33**, pp.580-592.
- [59] Humphrey, W., Dalke, A. and Schulten, K., 1996. VMD: visual molecular dynamics. *Journal of Molecular Graphics*, **14**, pp.33-38.
- [60] Cohen, G. and Heikkila, R.E., 1974. The generation of hydrogen peroxide, superoxide radical, and hydroxyl radical by 6-hydroxydopamine, dialuric acid, and related cytotoxic agents. *Journal of Biological Chemistry*, **249**, pp.2447-2452.
- [61] Veal, E.A., Day, A.M. and Morgan, B.A., 2007. Hydrogen peroxide sensing and signaling. *Molecular Cell*, **26**, pp.1-14.

- [62] Stone, J.R. and Yang, S., 2006. Hydrogen peroxide: a signaling messenger. *Antioxidants & Redox Signaling*, **8**, pp.243-270.
- [63] Zhou, Z.Y., Zhang, H.T. and Shi, Y., 2004. Theoretical study of the interactions between 1, 3-butanediol and hydrogen peroxide. *The Journal of Physical Chemistry A*, **108**, pp.6520-6526.
- [64] Su, Z. and Xu, Y., 2005. *Ab initio* study of chiral recognition in the propylene imine-hydrogen peroxide complex. *Physical Chemistry Chemical Physics*, **7**, pp.2554-2560.
- [65] Clancy, R.T., Sandor, B.J. and Moriarty-Schieven, G.H., 2004. A measurement of the 362 GHz absorption line of Mars atmospheric H₂O₂. *Icarus*, **168**, pp.116-121.
- [66] Encrenaz, T., Bézard, B., Greathouse, T.K., Richter, M.J., Lacy, J.H., Atreya, S.K., Wong, A.S., Lebonnois, S., Lefèvre, F. and Forget, F., 2004. Hydrogen peroxide on Mars: evidence for spatial and seasonal variations. *Icarus*, **170**, pp.424-429.
- [67] Encrenaz, T., Greathouse, T.K., Lefèvre, F. and Atreya, S.K., 2012. Hydrogen peroxide on Mars: observations, interpretation and future plans. *Planetary and Space Science*, **68**, pp.3-17.
- [68] Thompson, A.M., 1992. The oxidizing capacity of the earth's atmosphere: Probable past and future changes. *Science*, **256**, pp.1157-1165.
- [69] Vione, D., Maurino, V., Minero, C. and Pelizzetti, E., 2003. The atmospheric chemistry of hydrogen peroxide: A review. *Annali di Chimica*, **93**, p.477.
- [70] Cooper, W.J. and Zika, R.G., 1983. Photochemical formation of hydrogen peroxide in surface and ground waters exposed to sunlight. *Science*, **220**, pp.711-712.

- [71] Bulewicz, E.M. and Sugden, T.M., 1958. The recombination of hydrogen atoms and hydroxyl radicals in hydrogen flame gases. *Transactions of the Faraday Society*, **54**, pp.1855-1860.
- [72] He, S.Z., Chen, Z.M., Zhang, X., Zhao, Y., Huang, D.M., Zhao, J.N., Zhu, T., Hu, M. and Zeng, L.M., 2010. Measurement of atmospheric hydrogen peroxide and organic peroxides in Beijing before and during the 2008 Olympic Games: Chemical and physical factors influencing their concentrations. *Journal of Geophysical Research: Atmospheres*, **115**.
- [73] Kang, C.M., Han, J.S. and Sunwoo, Y., 2002. Hydrogen peroxide concentrations in the ambient air of Seoul, Korea. *Atmospheric Environment*, **36**, pp.5509-5516.
- [74] Liang, M.C., Hartman, H., Kopp, R.E., Kirschvink, J.L. and Yung, Y.L., 2006. Production of hydrogen peroxide in the atmosphere of a Snowball Earth and the origin of oxygenic photosynthesis. *Proceedings of the National Academy of Sciences*, **103**, pp.18896-18899.
- [75] Jackson, A.V. and Hewitt, C.N., 1999. Atmosphere hydrogen peroxide and organic hydroperoxides: a review. *Critical Reviews in Environmental Science and Technology*, **29**, pp.175-228.
- [76] Velikova, V., Yordanov, I. and Edreva, A., 2000. Oxidative stress and some antioxidant systems in acid rain-treated bean plants: protective role of exogenous polyamines. *Plant Science*, **151**, pp.59-66.
- [77] Richards, L.W., Anderson, J.A., Blumenthal, D.L., McDonald, J.A., Kok, G.L. and Lazrus, A.L., 1983. Hydrogen peroxide and sulfur (IV) in Los Angeles cloud water. *Atmospheric Environment*, **17**, pp.911-914.

- [78] Buckley, P.T. and Birks, J.W., 1995. Evaluation of visible-light photolysis of ozone-water cluster molecules as a source of atmospheric hydroxyl radical and hydrogen peroxide. *Atmospheric Environment*, **29**, pp.2409-2415.
- [79] Claeys, M., Wang, W., Ion, A.C., Kourtchev, I., Gelencsér, A. and Maenhaut, W., 2004. Formation of secondary organic aerosols from isoprene and its gas-phase oxidation products through reaction with hydrogen peroxide. *Atmospheric Environment*, **38**, pp.4093-4098.
- [80] Kroll, J.H. and Seinfeld, J.H., 2008. Chemistry of secondary organic aerosol: Formation and evolution of low-volatility organics in the atmosphere. *Atmospheric Environment*, **42**, pp.3593-3624.
- [81] Hua, W., Chen, Z.M., Jie, C.Y., Kondo, Y., Hofzumahaus, A., Takegawa, N., Chang, C.C., Lu, K.D., Miyazaki, Y., Kita, K. and Wang, H.L., 2008. Atmospheric hydrogen peroxide and organic hydroperoxides during PRIDE-PRD'06, China: their concentration, formation mechanism and contribution to secondary aerosols. *Atmospheric Chemistry and Physics*, **8**, pp.6755-6773.
- [82] Sakugawa, H., Kaplan, I.R., Tsai, W. and Cohen, Y., 1990. Atmospheric hydrogen peroxide. *Environmental Science & Technology*, **24**, pp.1452-1462.
- [83] Simon, A. and Feher, F., 1935. Raman effect and the constitution of hydrogen peroxide. *Ztschr Elektrochem.* **41**, p.290-3.
- [84] Massey, J.T. and Bianco, D.R., 1954. The Microwave Spectrum of Hydrogen Peroxide. *The Journal of Chemical Physics*, **22**, pp.442-448.

- [85] Hunt, R.H., Leacock, R.A., Peters, C.W. and Hecht, K.T., 1965. Internal-Rotation in Hydrogen Peroxide: The Far-Infrared Spectrum and the Determination of the Hindering Potential. *The Journal of Chemical Physics*, **42**, pp.1931-1946.
- [86] Helminger, P., Bowman, W.C. and De Lucia, F.C., 1981. A study of the rotational-torsional spectrum of hydrogen peroxide between 80 and 700 GHz. *Journal of Molecular Spectroscopy*, **85**, pp.120-130.
- [87] Helminger, P., Messer, J.K., Bowman, W.C. and De Lucia, F.C., 1984. Prediction and assignment of the FIR spectrum of hydrogen peroxide. *Journal of Quantitative Spectroscopy and Radiative Transfer*, **32**, pp.325-333.
- [88] Catalano, E. and Sanborn, R.H., 1963. On the Infrared Spectrum of Hydrogen Peroxide Matrix-Isolation Studies of the System H₂O₂:N₂ (II). *The Journal of Chemical Physics*, **38**, pp.2273-2276.
- [89] Pettersson, M., Tuominen, S. and Räsänen, M., 1997. IR spectroscopic study of H₂O₂, HDO₂, and D₂O₂ isolated in Ar, Kr, and Xe matrices. *The Journal of Physical Chemistry A*, **101**, pp.1166-1171.
- [90] Lundell, J., Pehkonen, S., Pettersson, M. and Räsänen, M., 1998. Interaction between hydrogen peroxide and molecular nitrogen. *Chemical Physics Letters*, **286**, pp.382-388.
- [91] Lundell, J., Jolkkonen, S., Khriachtchev, L., Pettersson, M. and Räsänen, M., 2001. Matrix Isolation and *Ab Initio* Study of the Hydrogen-Bonded H₂O₂-CO Complex. *Chemistry-A European Journal*, **7**, pp.1670-1678.

- [92] Goebel, J., Ault, B.S. and Del Bene, J.E., 2000. Matrix isolation and *ab initio* study of the hydrogen-bonded complex between H₂O₂ and (CH₃)₂O. *The Journal of Physical Chemistry A*, **104**, pp.2033-2037.
- [93] Engdahl, A. and Nelander, B., 2000. The structure of the water–hydrogen peroxide complex. A matrix isolation study. *Physical Chemistry Chemical Physics*, **2**, pp.3967-3970.
- [94] Goebel, J.R., Ault, B.S. and Del Bene, J.E., 2001. Matrix isolation and *ab initio* study of 1:1 hydrogen-bonded complexes of H₂O₂ with phosphorus and sulfur bases. *The Journal of Physical Chemistry A*, **105**, pp.11365-11370.
- [95] Goebel, J.R., Ault, B.S. and Del Bene, J.E., 2001. Matrix isolation and *ab initio* study of 1:1 hydrogen-bonded complexes of H₂O₂ with NH₃ and N(CH₃)₃. *The Journal of Physical Chemistry A*, **105**, pp.6430-6435.
- [96] Engdahl, A., Nelander, B. and Karlström, G., 2001. A matrix isolation and *ab initio* study of the hydrogen peroxide dimer. *The Journal of Physical Chemistry A*, **105**, pp.8393-8398.
- [97] Goebel, J.R., Antle, K.A., Ault, B.S. and Del Bene, J.E., 2002. Matrix Isolation and *ab Initio* Study of 1:1 Hydrogen-Bonded Complexes of H₂O₂ with HF, HCl, and HBr. *The Journal of Physical Chemistry A*, **106**, pp.6406-6414.
- [98] Engdahl, A. and Nelander, B., 2003. The binary complex between hydrogen peroxide and ozone: A matrix isolation study. *Chemical Physics*, **293**, pp.203-209.
- [99] Engdahl, A. and Nelander, B., 2004. The HOOH–HOO complex. A matrix isolation study. *Physical Chemistry Chemical Physics*, **6**, pp.730-734.

- [100] Pehkonen, S., Lundell, J., Khriachtchev, L., Pettersson, M. and Räsänen, M., 2004. Matrix isolation and quantum chemical studies on the H₂O₂–SO₂ complex. *Physical Chemistry Chemical Physics*, **6**, pp.4607-4613.
- [101] Mucha, M. and Mielke, Z., 2009. Photochemistry of the glyoxal–hydrogen peroxide complexes in solid argon: Formation of 2-hydroxy-2-hydroperoxyethanal. *Chemical Physics Letters*, **482**, pp.87-92.
- [102] Grzechnik, K., Mierzwicki, K. and Mielke, Z., 2013. Matrix-Isolated Hydrogen-Bonded and Van der Waals Complexes of Hydrogen Peroxide with OCS and CS₂. *Physical Chemistry Chemical Physics*, **14**, pp.777-787.
- [103] Jacob, D.J., 1986. Chemistry of OH in remote clouds and its role in the production of formic acid and peroxymonosulfate. *Journal of Geophysical Research: Atmospheres*, **91**, pp.9807-9826.
- [104] Khwaja, H.A., 1995. Atmospheric concentrations of carboxylic acids and related compounds at a semiurban site. *Atmospheric Environment*, **29**, pp.127-139.
- [105] Chebbi, A. and Carlier, P., 1996. Carboxylic acids in the troposphere, occurrence, sources, and sinks: A review. *Atmospheric Environment*, **30**, pp.4233-4249.
- [106] Khare, P., Kumar, N., Kumari, K.M. and Srivastava, S.S., 1999. Atmospheric formic and acetic acids: An overview. *Reviews of Geophysics*, **37**, pp.227-248.
- [107] Chameides, W.L. and Davis, D.D., 1983. Aqueous-phase source of formic acid in clouds. *Nature*, **304**, pp.427-429.

- [108] Stavrakou, T., Müller, J.F., Peeters, J., Razavi, A., Clarisse, L., Clerbaux, C., Coheur, P.F., Hurtmans, D., De Mazière, M., Vigouroux, C. and Deutscher, N.M., 2012. Satellite evidence for a large source of formic acid from boreal and tropical forests. *Nature Geoscience*, **5**, pp.26-30.
- [109] Chocholoušová, J., Špirko, V. and Hobza, P., 2004. First local minimum of the formic acid dimer exhibits simultaneously red-shifted O–H···O and improper blue-shifted C–H···O hydrogen bonds. *Physical Chemistry Chemical Physics*, **6**, pp.37-41.
- [110] Jakobsen, R.J., Mikawa, Y. and Brasch, J.W., 1967. Far infrared studies of hydrogen bonding in carboxylic acids—I formic and acetic acids. *Spectrochimica Acta Part A: Molecular Spectroscopy*, **23**, pp.2199-2209.
- [111] Kim, Y., Lim, S. and Kim, Y., 1999. The Role of a Short and Strong Hydrogen Bond on the Double Proton Transfer in the Formamidine–Formic Acid Complex: Theoretical Studies in the Gas Phase and in Solution. *The Journal of Physical Chemistry A*, **103**, pp.6632-6637.
- [112] Neuheuser, T., Hess, B.A., Reutel, C. and Weber, E., 1994. *Ab initio* calculations of supramolecular recognition modes. Cyclic versus noncyclic hydrogen bonding in the formic acid/formamide system. *The Journal of Physical Chemistry*, **98**, pp.6459-6467.
- [113] Dobado, J.A. and Molina, J.M., 1994. *Ab initio* molecular orbital study of the hydrogen peroxide-water complex (HOOH···H₂O). *The Journal of Physical Chemistry*, **98**, pp.1819-1825.
- [114] Mo, O., Yanez, M., Rozas, I. and Elguero, J., 1994. Structure, vibrational frequencies, and thermodynamic properties of hydrogen peroxide dimers: An *ab initio* molecular orbital study. *The Journal of Chemical Physics*, **100**, pp.2871-2877.

- [115] Boys, S.F. and Bernardi, F.D., 1970. The calculation of small molecular interactions by the differences of separate total energies. Some procedures with reduced errors. *Molecular Physics*, **19**, pp.553-566.
- [116] Pettersson, M., Maçôas, E.M.S., Khriachtchev, L., Lundell, J., Fausto, R. and Räsänen, M., 2002. Cis→trans conversion of formic acid by dissipative tunneling in solid rare gases: Influence of environment on the tunneling rate. *The Journal of Chemical Physics*, **117**, pp.9095-9098.
- [117] Willemot, E., Dangoisse, D. and Bellet, J., 1978. Microwave spectrum of formic acid and its isotopic species in D, ^{13}C and ^{18}O . Study of Coriolis resonances between ν_7 and ν_9 vibrational excited states. *Journal of Molecular Spectroscopy*, **73**, pp.96-119.
- [118] Priem, D., Ha, T.K. and Bauder, A., 2000. Rotational spectra and structures of three hydrogen-bonded complexes between formic acid and water. *The Journal of Chemical Physics*, **113**, pp.169-175.
- [119] Coudert, L.H., Lovas, F.J., Suenram, R.D. and Hougen, J.T., 1987. New measurements of microwave transitions in the water dimer. *The Journal of Chemical Physics*, **87**, pp.6290-6299.
- [120] The script (licensed at MIT) and user guide are accessible on GitHub:
<https://github.com/leoyli/frequency-loop-permutator>.
- [121] Dyke, T.R., Howard, B.J. and Klemperer, W., 1972. Radiofrequency and microwave spectrum of the hydrogen fluoride dimer; a nonrigid molecule. *The Journal of Chemical Physics*, **56**, pp.2442-2454.

- [122] Balasubramanian, K., 2004. Nonrigid group theory, tunneling splittings, and nuclear spin statistics of water pentamer:(H₂O)₅. *The Journal of Physical Chemistry A*, **108**, pp.5527-5536.
- [123] Evangelisti, L., Gou, Q., Feng, G., Caminati, W., Mead, G.J., Finneran, I.A., Carroll, P.B. and Blake, G.A., 2017. Conformational equilibrium and internal dynamics in the isopropanol–water dimer. *Physical Chemistry Chemical Physics*, **19**, pp.568-573.
- [124] Meyer, R., 1979. Flexible models for intramolecular motion, a versatile treatment and its application to glyoxal. *Journal of Molecular Spectroscopy*, **76**, pp.266-300.
- [125] Meyer, R. and Caminati, W., 1991. Quartic centrifugal distortion constants derived from a flexible model for 3-methylthietan. *Journal of Molecular Spectroscopy*, **150**, pp.229-237.
- [126] Evangelisti, L., Écija, P., Cocinero, E.J., Castaño, F., Lesarri, A., Caminati, W. and Meyer, R., 2012. Proton tunneling in heterodimers of carboxylic acids: A rotational study of the benzoic acid–formic acid bimolecule. *The Journal of Physical Chemistry Letters*, **3**, pp.3770-3775.
- [127] Albert, S., Albert, K.K., Hollenstein, H., Tanner, C.M. and Quack, M., 2011. Fundamentals of rotation–vibration spectra. *Handbook of High-resolution Spectroscopy*.
- [128] Pearson, J.C., Sastry, K.V.L.N., Herbst, E. and De Lucia, F.C., 1996. The Millimeter-and Submillimeter-Wave Spectrum of Gauche-Ethyl Alcohol. *Journal of Molecular Spectroscopy*, **175**, pp.246-261.
- [129] Watson, J.K., 1977. Aspects of quartic and sextic centrifugal effects on rotational energy levels. *Vibrational spectra and structure*, **6**, pp.1-89.

- [130] Savin, A., Nesper, R., Wengert, S. and Fässler, T.F., 1997. ELF: The electron localization function. *Angewandte Chemie International Edition*, **36**, pp.1808-1832.
- [131] Espinosa, E., Molins, E. and Lecomte, C., 1998. Hydrogen bond strengths revealed by topological analyses of experimentally observed electron densities. *Chemical Physics Letters*, **285**, pp.170-173.
- [132] Nikolaienko, T.Y., Bulavin, L.A. and Hovorun, D.M., 2012. Bridging QTAIM with vibrational spectroscopy: The energy of intramolecular hydrogen bonds in DNA-related biomolecules. *Physical Chemistry Chemical Physics*, **14**, pp.7441-7447.
- [133] Grabowski, S.J. ed., 2006. *Hydrogen bonding: new insights (Vol. 3)*. Dordrecht: Springer.
- [134] Saxena, P. and Hildemann, L.M., 1996. Water-soluble organics in atmospheric particles: A critical review of the literature and application of thermodynamics to identify candidate compounds. *Journal of Atmospheric Chemistry*, **24**, pp.57-109.

APPENDICES

Appendix A – The Cartesian coordinates of the optimized geometry for HP–FA–I and HP–FA–I calculated at the MP2/6-311++g(2d,p) level of theory.*

(a) HP–FA–I:

Atoms	x	y	z
C	1.618647	- 0.153967	- 0.006127
O	0.934324	- 1.152675	0.125865
H	2.711655	- 0.182165	- 0.051767
O	1.164728	1.088148	- 0.111690
H	0.176673	1.064255	- 0.048848
H	- 1.988562	0.820885	0.983078
O	- 1.562345	0.766729	0.113524
O	- 1.780985	- 0.640917	- 0.198401
H	- 0.867045	- 0.982381	- 0.067835

(b) HP–FA–I*:

Atoms	x	y	z
C	-1.624590	-0.126694	-0.005846
O	-0.953825	-1.120005	-0.210582
H	-2.717946	-0.143816	0.044641
O	-1.163621	1.105572	0.186107
H	-0.183120	1.096842	0.106190
H	2.456844	0.905271	-0.451706
O	1.537483	0.663995	-0.271420
O	1.743242	-0.655324	0.329935
H	0.885531	-1.052042	0.063637

Appendix B – Python 3 script for running the closed-frequency loop permutations. [120]

```
# Author    : Leo Y. Li
# Licence   : MIT
# Version   : 1.1.2

def checkLoop(inputList, deviations=0.02, minimumSeparations=0, rounded=True, instantOutput=False,
reportRates=250):
    # option insurance
    deviations = abs(deviations)
    reportRates = abs(reportRates)
    minimumSeparations = abs(minimumSeparations)

    # Initialize a blank array for result storage
    global recordBook
    recordBook = []

    # Clean & Sort the input file (from small to large value)
    if rounded:
        inputList = list(set([round(n, 3) for n in inputList]))
    inputList = sorted(inputList)
    length = len(inputList)

    # initial reports
    print("Lines to be permuted:", length)

    # permutation
    for A in range(length):
        if A % reportRates == 0:
            # progression reports
            print("\ncalculating... currently at", A, "-th line in the sequence.")
        for B in range(A + 1, length):
            if (inputList[B] - inputList[A]) < minimumSeparations:
                continue
            for C in range(B + 1, length):
                if (inputList[C] - inputList[B]) < minimumSeparations:
                    continue
                for D in range(C + 1, length):
                    if (inputList[D] - inputList[C]) < minimumSeparations:
                        continue
```

```

# check criteria for a loop
errors = round(abs(inputList[D] - inputList[C] - inputList[B] + inputList[A]), 4)
if errors <= deviations:
    newFoundLoop = [inputList[D], inputList[C], inputList[B], inputList[A], errors]
    recordBook.append(newFoundLoop)
    if instantOutput:
        print(", ".join('{:9.3f}'.format(i) for v, i in enumerate(newFoundLoop)))

# final reports
if not instantOutput:
    result()
else:
    print("\nALL DONE! Numbers of loop being found:", len(recordBook))
    print("To show all found loops, command 'result()' before making another permutation.")

def result():
    print("\nAll found closed frequencies loops:\n", "_"*75, "\n\n\t#1,\t\t#2,\t\t#3,\t\t#4,\t
errors\n", "_"*75, "\n")
    for n in range(len(recordBook)):
        print(",\t".join('{:10.3f}'.format(i) for v, i in enumerate(recordBook[n])))
    print("", "_"*75, "\n {:>70}".format("Total:"), len(recordBook))

```